A novel methodology to estimate hydrogen diffusivity and its applications in revealing hydrogen effects in CoCrNi medium-entropy alloy versus 316L stainless steel

Dong-Hyun Lee[1,*], Yun Hee An[1], Yakai Zhao[2,*], Ju Hyeok Lee[1], Hyun You Kim[1],
You Sub Kim[1], Soo Yeol Lee[1]

[1]Department of Materials Science and Engineering, Chungnam National University, Daejeon 34134, Republic of Korea
[2]Institute of Materials Research and Engineering, Agency for Science, Technology and Research, Singapore 138634, Republic of Singapore

*Corresponding authors: dhlee@cnu.ac.kr (D.-H. Lee); zhaoyk@imre.a-star.edu.sg (Y. Zhao)

Abstract

Hydrogen diffusivity is one of the important factors affecting the susceptibility to hydrogen embrittlement of metals and alloys. Here, we proposed a novel approach to estimate hydrogen diffusivity in FCC alloys by performing nanoindentation experiments with continuous stiffness measurement. In consideration of the plastic zone size around the indentation, the relationship between hydrogen-induced hardness change and the depth from the sample surface was established for two typical FCC alloys—316L stainless steel (SS) and CoCrNi medium-entropy alloy (MEA)—subjected to hydrogen-charging and subsequent room-temperature aging. By combining with the estimation of the through-thickness distribution of hydrogen concentration, hydrogen diffusivity values were successfully determined, which agreed well with the literature data. It was revealed that CoCrNi MEA exhibited a hydrogen diffusivity ~0.68 times higher than that in SS316L, and that hydrogen-induced softening upon long-term aging (at room temperature) was observed in CoCrNi but not in SS316L. The underlying mechanisms for the distinct hydrogen-related phenomena in CoCrNi MEA were elucidated based on the density functional theory calculations of hydrogen solution energy and vacancy formation energy.

Keywords: nanoindentation; hardness; hydrogen diffusivity; face-centered cubic; stainless steel; medium-entropy alloy.

1. Introduction

As a clean energy carrier alternative to conventional fossil fuels, hydrogen is increasingly demanded and utilized, acting an important role as part of the “net zero” carbon strategy worldwide (Cullen, 2021; Zhao, 2020). Nevertheless, wide application of hydrogen energy is hampered by the great challenges in the storage and transportation of hydrogen gas (or liquid), since the diffusible hydrogen atoms in metals could lead to serious deterioration in mechanical properties, especially ductility and toughness (so-called “hydrogen embrittlement”) (An, 2020; Isfandbod and Martínez-Pañeda, 2021; Li, 2020). Hydrogen atoms tend to concentrate at crystalline defects such as grain boundaries (Lee, 2022a; Zhou, 2016), dislocations (San Marchi, 2007; Zhu, 2017), vacancies (Li, 2015), and interfaces (Tarzimoghadam, 2016; Zhang, 2019), resulting in crack initiation and propagation along them (Lee, 2023, 2019). More specifically, at or near crack tip, hydrogen diffusivity is the rate-limiting factor strongly affecting how fast hydrogen atoms accumulate ahead of crack tip and hence the crack growth rate (Abdolvand, 2019; Lee, 2021). In this context, the susceptibility to hydrogen embrittlement of metals and alloys is closely correlated with hydrogen diffusivity, since a low hydrogen diffusivity inhibits the severe hydrogen accumulations at critical sites (e.g., crystalline defects and crack tip) and hence reduces the embrittlement.

On this basis, medium-/high-entropy alloys (M/HEAs) with face-centered cubic (FCC) structure offer potentials as hydrogen-resistant alloys due to their excellent mechanical performances (Chandan, 2022; Gludovatz, 2014; Li, 2023; Miracle and Senkov, 2017; Wei, 2022; Zhang., 2023) combined with sluggish hydrogen diffusion (Li, 2022c; Ren, 2019; Xie, 2021). Recently, it has been reported that hydrogen diffusion in M/HEAs could be further retarded by increasing the concentration of Cr (Marques, 2021), Co, or Mn (Zhou, 2022) elements. In this regard, tailoring chemical composition for impeding hydrogen diffusion could be a promising strategy for designing M/HEAs with prominent resistance to hydrogen embrittlement.

In order to evaluate the hydrogen diffusivity, conventionally either gaseous or electrochemical permeation tests were employed. The former is conducted in a highly pressurized hydrogen gas environment and usually at a high temperature (San Marchi, 2007; Tsong-Pyng and Altstetter, 1986; Xiukui, 1989), whereas the latter is carried out in an electrolytic solution at (or near) room temperature (RT) (Arantes, 1993; Brass and Chanfreau, 1996; Lin, 2020). However, there exist drawbacks in both methods. Gaseous permeation experiment is only appropriate to measure hydrogen diffusivity at elevated temperatures (e.g., $T > 673$ K). The hydrogen diffusivity in a broad range at or near RT, which is often the service temperature for hydrogen storage or transportation, can only be extrapolated from elevated temperature data but not directly measured. On the other hand, electrochemical hydrogen permeation can be performed at RT to obtain the hydrogen diffusivity due to its high hydrogen fugacity at the reaction surface (Liu, 2014; Zhao, 2019). Nevertheless, for FCC alloys having extremely low hydrogen diffusivity at RT (~10^{-16} m^2/s for austenitic steels (San Marchi, 2007)), the penetration of hydrogen through the whole sample can be rather time-consuming; for example, it takes ~33 h for 316L stainless steel with the thickness of ~0.5 mm (Lin, 2020). Therefore, the thickness of the sample for electrochemical permeation has to be as thin as possible, which in turn increases the complexity and difficulty in sample preparation.

Small-scale mechanical testing methods, especially nanoindentation, have emerged as valuable tools in hydrogen-related research. These methods have been utilized in both *ex-situ* (Gao, 2022; Lee, 2014a; Park, 2021; Zhao, 2015, 2017a, 2017b) and *in-situ* hydrogen environments (Deng and Barnoush, 2018; Ebner, 2021; Soundararajan, 2023), providing insights into the effects of hydrogen on hardness (Kim and Tasan, 2019; Lee., 2014a; Park, 2021), strain-rate sensitivity (Ebner, 2021; Hong, 2019a), elastic-to-plastic transition (Lu, 2019; Soundararajan, 2023; Wang, 2022), and creep deformation (Hong, 2019b). Additionally, the small-scale testing capability of nanoindentation enables direct characterizing the microstructural features (e.g., constituent phases, grain boundary) and hence identify their respective roles in affecting hydrogen embrittlement. For instance, Gao *et al*. (2022) utilized nanoindentation for identifying the hydrogen-sensitive phase in the dual-phase $Al_{0.7}CoCrFeNi$ HEA, from which FCC phase is found more susceptible to hydrogen-induced hardening than the body-centered cubic (BCC) phase does (Gao, 2022). However, most nanoindentation studies on hydrogen effects tend to focus solely on the mechanical properties obtained at a given indentation depth, yet often overlooking the potentials of utilizing nanoindentation to analyze the depth-sensitive changes in hardness. By using continuous stiffness measurement (CSM) mode, the variations in hardness with depth can be readily obtained from a single indentation (Oliver and Pharr, 1992, 2004). Therefore, if nanoindentation tests were carried out on the electrochemically charged sample, where a gradient of hydrogen concentration is generally steep from the surface (Lee, 2021; Zhao, 2015, 2019), the variation in hardness along the indentation depth could be correlated with an inhomogeneous hydrogen distribution. This may empower nanoindentation to analyze the hydrogen diffusion behavior (e.g., hydrogen penetration depth or eventually hydrogen diffusivity), leading to a simultaneous understanding of both hydrogen diffusivity and its effect on the mechanical behavior.

Keeping these in view, the present work was initiated to investigate the feasibility of employing nanoindentation to estimate hydrogen diffusivity at or near RT. This approach has the potential to overcome the limitations associated with traditional hydrogen permeation tests, particularly the requirement of extremely thin sample. We performed nanoindentation experiments on the electrochemically charged 316L stainless steel (SS316L) and CoCrNi medium entropy alloy (MEA). These two alloys were selected as the target materials in present study because: (1) they both possess single-phase FCC structure and share rather similar constituting elements (especially, Cr and Ni are the main elements—in addition to Fe—in austenitic SSs including 316L) (Miracle and Senkov, 2017; Zhao, 2017b), and (2) they both have been reported to possess excellent mechanical performances at both cryogenic temperature and hydrogen environment (Gludovatz, 2016; Kim, 2021; Soundararajan, 2020; Zhang, 2008). Both alloys were fabricated by direct energy deposition (DED) since additive manufacturing (AM) has been proven to offer better mechanical properties as well as comparable (or even better) resistance to hydrogen embrittlement than conventional manufacturing does (Lee, 2021; Park, 2021). First, we examined how the hydrogen effect on hardness varies with indentation depth (or hydrogen content) in SS316L and CoCrNi MEA. Then, we suggested a novel way to estimate hydrogen diffusivity through nanoindentation experiment, and applied it to SS316L and CoCrNi MEA. The difference in hydrogen diffusivity as well as the distinct hardening vs. softening behaviors between these two alloys are discussed in terms of the hydrogen solution energy and vacancy formation energy calculated via density functional theory (DFT). The present study provides fundamental insights into hydrogen diffusivity and its effects on hydrogen embrittlement in FCC alloys, and demonstrates the effectiveness of nanoindentation technique for this purpose.

2. Materials and experimental

Gas-atomized spherical powders with the diameter of ~50–150 μm were utilized to fabricate CoCrNi and SS316L blocks (13 × 13 × 100 mm^3 each, in size) using commercial DED equipment, MX-400 (INSSTEK). DED process was conducted under Ar gas atmosphere, a laser power of 380–400 W, a scan speed of 14 mm/s, a spot size of 0.8–1.2 mm, a powder feed rate of 0.04 g/s, a layer thickness of 250 μm, and a hatch spacing of 400 μm. The chemical compositions of the as-built samples were confirmed by energy dispersive X-ray spectroscopy (EDS) and the results are listed in Table 1. The as-built samples were machined along the plane parallel to the build direction, and all the subsequent experiments were conducted on the side surface of the blocks. The specimens were mechanically polished with the SiC papers and subsequently with 0.05 μm colloidal silica. Then, the surfaces were vibration-polished for 24 h with 0.02 μm colloidal silica to remove any possible surface damage induced during prior polishing. The microstructures of the specimens were characterized using an electron backscattered diffraction (EBSD) mounted on a scanning electron microscope (SEM; Merlin Compact, Carl Zeiss) as well as electron channeling contrast imaging (ECCI).

Table 1. Chemical compositions (wt.%) of the DED fabricated CoCrNi and SS316L samples investigated in this study.

Material	Co	Cr	Ni	Mo	Mn	Si	Fe
CoCrNi	33.7	30.5	35.7	-	-	-	-
SS316L	-	17.2	13.8	2.3	1.0	0.7	Bal.

Hydrogen was electrochemically introduced into the sample by cathodic charging at RT with potentiostat using a 0.05M H_2SO_4 solution with 2 g/l CH_4N_2S. Hydrogen charging was conducted at a constant current density of 4 mA/cm^2 for two different charging times, $t_c = 30$ and 120 min. Additionally, the hydrogen charged specimens were naturally aged in ambient atmosphere at RT for different time spans, $t_a = 50$, 90, 130, and 1440 min, respectively, so as to let the hydrogen diffuse out of the samples and thus investigate the effect of hydrogen outgassing on hardness. Hereafter, the sample charged for *X* min and subsequently RT-aged for *Y* min will be referred to as “*X*C*Y*A”. Thus, for example, a sample charged for 120 min and then RT-aged for 50 min will be “120C50A” sample. Nanoindentation experiments were performed on the uncharged and hydrogen-charged specimens using iMicro Nanoindenter (KLA) equipped with Berkovich tip at a peak load $P_{max} = 50$ mN and constant indentation strain rate $(dh/dt)/h = 0.025$ s^{-1} (where *h* and *t* are indentation depth and time, respectively). Here, CSM module (Oliver and Pharr, 2004), which allows to obtain hardness (*H*) values continuously as a function of *h* from single nanoindentation, was utilized. At least 10 indentations were conducted for each condition, which were finished within 30 min to minimize the potential influence from hydrogen outgassing in the hydrogen-charged samples. The spacing between indentations was set as 100 μm so that multiple grains were included to obtain the orientation-independent response of the material.

The amount of absorbed hydrogen was measured by recourse to thermal desorption spectroscopy (TDS; G4 Phoenix, Bruker). Various heating rates (Φ) from 300 to 500 K/h were utilized for the TDS measurements. The total hydrogen content was determined by measuring the cumulative amount of the desorbed hydrogen from RT up to 400 °C.

To investigate the interaction between hydrogen atom and the interstitial sites, spin-polarized DFT calculations were performed using a plane-wave basis with the VASP code (Kresse and Furthmüller, 1996; Kresse and Joubert, 1999). The exchange-correlation energy of the Kohn-Shan equation was estimated with the generalized gradient approximation (GGA)-level functional proposed by Perdew, Burke, and Ernzerhoff (PBE) (Perdew, 1996). The interaction between the ionic core and the valence electrons was described by the projector augmented wave method (Blöchl, 1994). Valance electron wave functions were expanded on a plane-wave basis up to an energy cutoff of 270 eV. A 3×3×2 supercell with 72 atoms was utilized for both CoCrNi and SS316L alloys. Their chemical compositions displayed in Table 1 were taken into consideration when selecting the number of constituent elements. The specific numbers of constituent elements within a 3×3×2 cell are provided in Table S1 in Supplementary Information (SI). The convergence criteria for the electronic structure and the atomic geometries were 10^{-4} eV and 0.05 eV/Å, respectively. A Fermi smearing function with a finite temperature width of 0.2 eV was utilized to improve the convergence of states near the Fermi level (Kratzer and Neugebauer, 2019). The location of the transition state within the diffusion pathway of a hydrogen atom in bulk lattice was estimated with the climbing-image nudge elastic band method (CI-NEB) (Henkelman, 2000; Henkelman and Jónsson, 2000).

The hydrogen solution energy, $E_{\text{H-sol}}$, is calculated using:

$$E_{H-sol} = E_{H+bulk} - E_{bulk} - \frac{1}{2}E_{H_2} \quad (1)$$

where E_{bulk} and $E_{\mathrm{H+bulk}}$ are the total energies of relaxed configurations of the perfect lattice and the lattice embedding one hydrogen atom, respectively. E_{H_2} is the energy of H_2 in a vacuum (i.e., −6.76 eV). In addition, DFT calculation was utilized to investigate the change in formation energy of vacancy due to hydrogen atom. For this, the formation energy of vacancy, ΔE_{vac}, was calculated using:

$$\Delta E_{vac} = E_{vac,bulk} - E_{bulk} + E_{atom} \quad (2)$$

where $E_{\mathrm{vac,bulk}}$ and E_{atom} are the total energies of relaxed lattice with one vacancy and the one atom, respectively.

3. Results

3.1. Microstructure

The microstructures of DED CoCrNi MEA and SS316L characterized by EBSD and ECCI are shown in Fig. 1. The inverse pole figure map of CoCrNi MEA(Fig. 1a) reveals that most grains grew along the building direction and a large fraction of low-angle grain boundaries (misorientation in the range of 2–15°) are formed within the grains. The average grain size is estimated to be ~460 μm measured by counting only high-angle grain boundaries (misorientation >15°). Fig. 1b displays the ECCI images of the CoCrNi MEA, showing that there exists a solidification cellular substructure with the size of ~1–2 μm in diameter inside the grains. Furthermore, high-density yet sparsely-distributed dislocations can be found in CoCrNi MEA (Fig. 1c). There seems to be no well-developed dislocation arrangement (e.g., in cellular shape as widely observed in many LPBF alloys (Wang, 2018)) in the current DED-fabricated alloys, which may be a result of limited thermal cycles during DED under certain conditions (Li, 2022a, 2022b). As shown in Figs. 1d–1f, the initial microstructure of SS316L is very similar to that of CoCrNi MEA except for the grain size (~270 μm for SS316L).

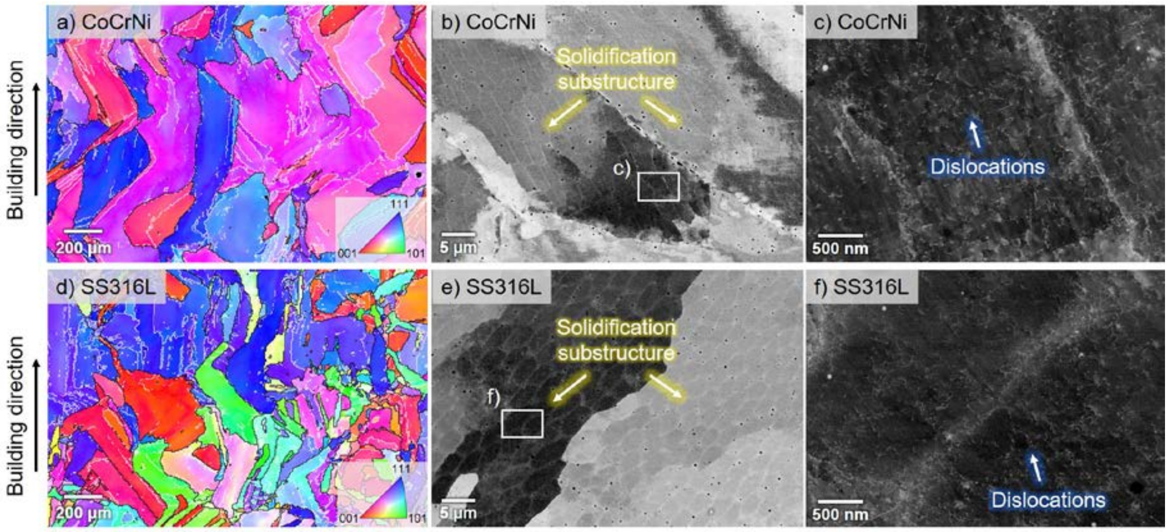

Fig. 1 Micorstructure of the DED fabricated (a–c) CoCrNi MEA and (d–f) SS316L samples: (a) and (d) display the EBSD inversece pole figure maps; (b–c) and (e–f) show ECCI images.

3.2. Hydrogen-induced nanohardness variations

Fig. 2a presents the results from nanoindentation tests conducted on CoCrNi MEA. Nanoindentation hardness (H_N) values were estimated by CSM according to Oliver-Pharr method (Oliver and Pharr, 1992), and the obtained H_N values are given as a function of displacement (h). Fig. 2a shows that hydrogen charging induces hardening behavior in CoCrNi MEA especially for large h regime, but it becomes less pronounced with increasing aging time. By contrast, for small h regime (< 200 nm), hydrogen-induced softening behavior is observed as shown in the inset of Fig. 2a. To more clearly capture the hydrogen effect on H_N, the change in H_N due to hydrogen charging ($\Delta H_N = H_{N,XCYA} - H_{N,UC}$) is provided as a function of h in Fig. 2b. Note that ΔH_N was calculated by using $H_{N,XCYA}$ and $H_{N,UC}$ values at the same h to avoid indentation size effect which manifests as an increase in H_N with decreasing h. The ΔH_N value monotonically increases from negative to positive as h increases, suggesting that a transition from hydrogen-induced softening to hardening indeed occurs. With increasing aging time, the threshold h value at which softening-to-hardening transition occurs increases and the amount of hydrogen-induced hardening decreases. This implies that hydrogen-induced hardening becomes less pronounced as aging time (or equivalently the amount of hydrogen desorption) increases. Furthermore, when the aging time is prolonged to 2880 min, only hydrogen-induced softening prevailed for the whole investigated h.

In contrast to CoCrNi MEA, a hydrogen-induced hardening is consistently observed in SS316L for the whole h range investigated (Fig. 2c), which is confirmed by the ΔH_N variation shown in Fig. 2d. Another important feature in Fig. 2d is that, for the SS316L sample with 120C50A condition, a clear rise in ΔH_N occurs with a maximum ΔH_N of ~2.95 GPa at h = ~200 nm and then ΔH_N starts to decrease with further increase in h. Similar hardening behavior was also observed for the other aged samples (120C90A and 120C130A), but the amount of hardening decreases with increasing aging time. On the other hand, 120C2880A condition shows almost negligible ΔH_N, indicating that the hydrogen atoms introduced in the SS316L almost all desorbed after long-term aging. Even in this case, hydrogen-charging led to a slight increase in hardness for $h < 150$ nm (Fig. 2d). Considering that hydrogen-charging itself induced high density of stacking faults and slip steps on the hydrogen-exposed surface (Fig. S1 in SI), such hardening is mainly attributed to the charging-induced deformation. Despite the charging-induced deformation, however, CoCrNi MEA showed hydrogen-induced softening for all investigated depths for the 120C2880A condition. This suggests that the softening effect predominates over the effect of the marginal charging-induced deformation in the CoCrNi MEA.

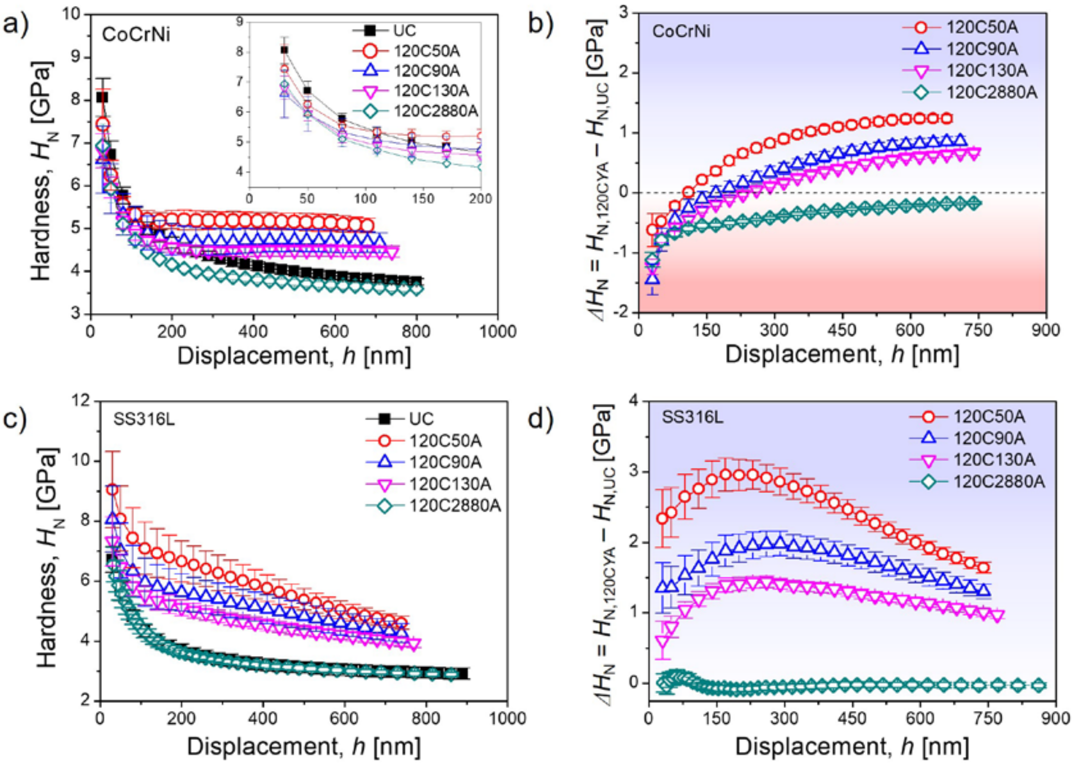

Fig. 2 Nanoindentation results on (a,b) CoCrNi MEA and (c,d) SS316L samples; (a) and (c) variations in nanoindentation hardness, H_N, with displacement; (b) and (d) change in H_N due to hydrogen-charging ($\Delta H_N = H_{N,120CYA} - H_{N,UC}$) vs. displacement.

To gain more insights into the influence of hydrogen desorption on H_N, the variation in H_N as a function of aging time was investigated. The results obtained for CoCrNi MEA and SS316L are summarized in Figs. 3a and 3b, respectively. Note that H_N values in Fig. 3 was obtained from h ~700 nm where hydrogen-induced hardening behavior is predominant for the short-term aging. As shown in Fig. 2, H_N increment due to hydrogen markedly reduces upon aging of hydrogen charged samples. In the case of CoCrNi MEA, H_N decreases to that of the UC condition after t_a ~360 min and aging beyond 360 min leads to a further reduction in H_N, that is, hydrogen-induced softening occurs for t_a > 360 min. For SS316L, however, H_N of hydrogen charged sample decreases to that of the UC sample after much longer t_a (i.e., ~1440 min) and, more importantly, further reduction in H_N does not occur even after prolonged t_a. In order to check whether the results in Fig. 3 is an artifact or not, the Meyer’s hardness values by directly measuring the area of nanoindentation impression from a SEM images (as shown in Fig. 4), $H_{\mathrm{N,SEM}}$, were obtained (Lee, 2022b; Zhao, 2014). As listed inside the images in Fig. 4, the $H_{\mathrm{N,SEM}}$ values also verify that the hydrogen-induced softening behavior happens only in CoCrNi MEA and not in SS316L.

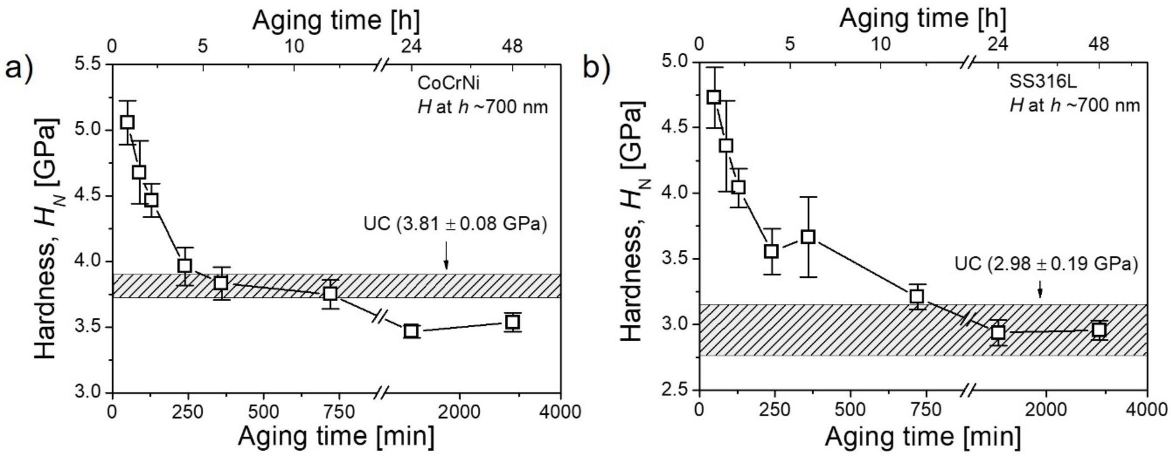

Fig. 3 Variation in nanoinndentation hardness as a function of aging time. The hardness values presented were those obtained at ~700 nm where hydrogen-induced hardening predominates for the short-term aging.

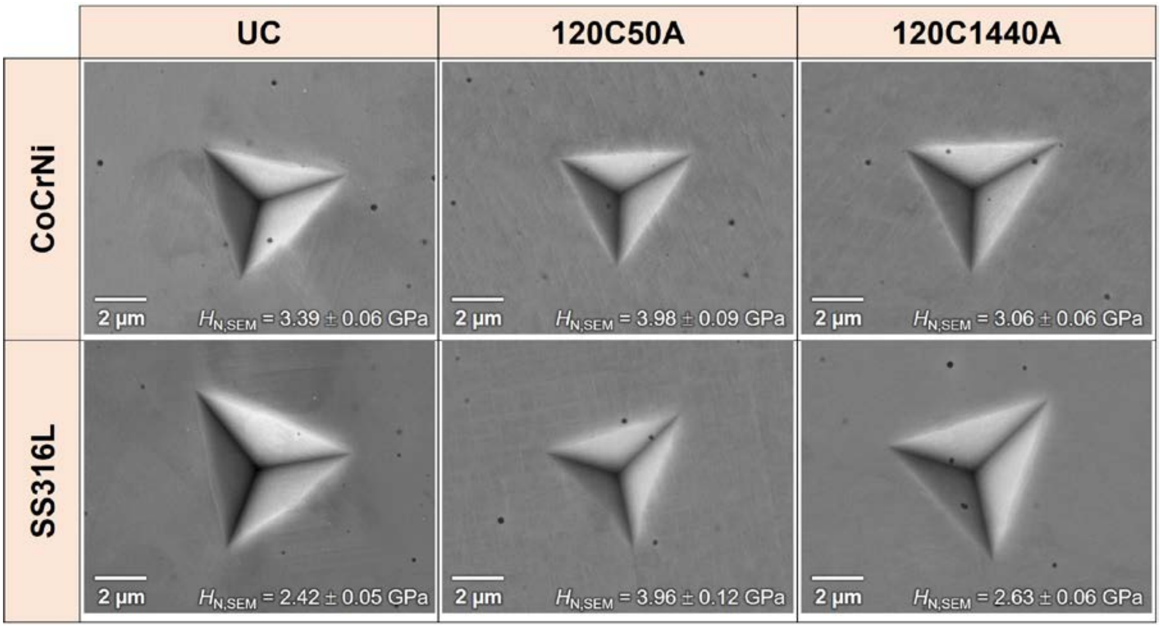

Fig. 4 Representative SEM micrographs of nanoindentation impressions for (a–c) CoCrNi MEA and (d–f) SS316L.

3.3. Hydrogen desorption behavior

TDS analysis was employed to analysis the hydrogen solubility and trapping behavior of the CoCrNi MEA and SS316L. The hydrogen desorption curves for the two samples with hydrogen charging for 120 min (i.e., 120C) are shown in Fig. 5a and 5b. Both CoCrNi MEA and SS316L exhibit a single desorption peak, and the peak temperatures shifts to higher values with increasing heating rate Φ. The CoCrNi MEA contains slightly higher hydrogen content than the SS316L (~9.3 wt. ppm vs. ~7.9 wt. ppm, at $\Phi = 400$ K/h). To understand the effect of aging, TDS analysis was also employed on the two samples in 120C1440A condition and the resultant desorption curves obtained at $\Phi = 400$ K/h are summarized in Fig. 5c. After room temperature aging for 1440 min, almost all the charged hydrogen atoms detrap and diffuse out of the CoCrNi MEA and thus the amount of remaining hydrogen is merely ~0.3 wt. ppm. For the SS316L, on the other hand, the remaining hydrogen after aging is ~0.9 wt. ppm, indicating that the extent of aging-induced hydrogen desorption is lower in the SS316L (~7.0 wt. ppm), compared to the CoCrNi MEA (~9.0 wt. ppm). Kissinger analysis (Kissinger, 1957) was applied in order to determine the activation energy (E_a) for hydrogen desorption (Kissinger, 1957):

$$\frac{\partial\left(ln\left({}^{\Phi}/_{T_P^2}\right)\right)}{\partial\left({}^{1}/_{T_P}\right)} = -\frac{E_a}{R} \tag{3}$$

where T_P is the temperature corresponding to the maximum value of each desorption peak and R is the gas constant. As shown in Fig. 5d, E_a can be readily obtained from the slope of the linear fitting, and the estimated E_a values for CoCrNi MEA and SS316L are ~22.3 and ~39.5 kJ/mol, respectively. A lower E_a value in CoCrNi suggests that the interaction between hydrogen and hydrogen trapping sites is slightly weaker in it than in SS316L. Considering the relatively low E_a value, the possible hydrogen trapping sites in these two alloys might be interstitial lattice sites, dislocations (27–58 kJ/mol (Ryu, 2012), grain boundaries (20.5 kJ/mol (Lee and Lee, 1986)). In FCC metals and alloys, since the hydrogen diffusion is comparable or even slower than the detrapping process, the rate-controlling stage for the thermal desorption process during TDS is H diffusion and the desorption peak at relatively low temperatures is a combinational outcome from both hydrogen diffusion as well as detrapping from weak trapping sites (e.g. dislocations and grain boundaries).

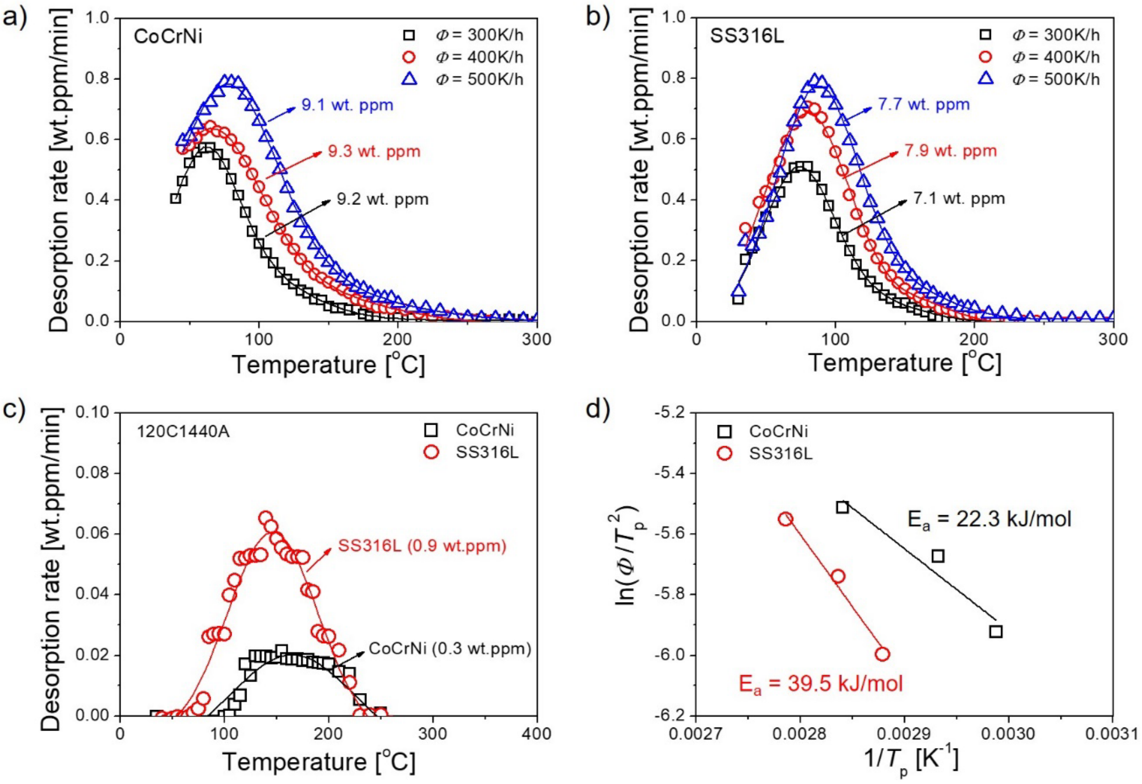

Fig. 5 Results of TDS analysis: (a–c) variations in hydrogen desorption rate with temperature; (d) calculation of activation energy for desorption using Kissinger equation.

4. A novel methodology to estimate hydrogen diffusivity via nanoindentation

It has been widely reported that FCC metals and alloys exhibited a steep gradient in hydrogen content through the thickness of the sample when hydrogen is electrochemically introduced, which is mainly attributed to the low hydrogen diffusivity in these alloys (Lee, 2021; Zhao, 2019). Such a variation in hydrogen content across thickness, nevertheless, offers an opportunity to estimate the hydrogen diffusivity in an alloy if one can measure/calculate the hydrogen content profile (vs. distance from the charging surface) in a reasonably accurate manner. When exposed to hydrogen environment, hydrogen permeation into the materials is largely controlled by diffusion that is governed by Fick's second law:

$$\frac{\partial C_H}{\partial t} = D_H \frac{\partial^2 C_H}{\partial x^2} \tag{4}$$

where C_H is local hydrogen concentration, x is the distance from the surface, t is the time, and

D_H is the diffusion coefficient of hydrogen. Under the assumption that the initial hydrogen concentration is negligible and the surface concentration, C_s, is constant, C_H during hydrogen charging is given as (Zhao, 2017b)

$$C_H(x, t_c)/C_S = \left[1 - erf\left(\frac{x}{2\sqrt{D_H t_c}}\right)\right] \tag{5}$$

where t_c is hydrogen charging time and *erf* represents the Gauss error function. The C_H/C_S profiles in the samples according to Eq. (5) are illustrated in Fig. 6a where three distinct D_H values ($D_{H,1} < D_{H,2} < D_{H,3}$) are considered. It is evident that hydrogen is mostly concentrated near the surface and, more importantly, both maximum hydrogen permeation depth and C_H (at a given x) increase as D_H increases. The change in C_H upon aging of hydrogen charged sample can also be estimated by considering Eq. (4). In the case of aging, C_H values at the end of hydrogen charging, which was calculated by Eq. (5) with $t = t_c$, were set as the initial condition (IC), and $C_H(0,t_a) = 0$ was imposed as a boundary condition (BC):

$$\left.\begin{array}{ll} C_H(x, 0)/C_S = \left[1 - erf\left(\frac{x}{2\sqrt{D_H t_c}}\right)\right] & (IC) \\ C_H(0, t_a) = 0 & (BC) \end{array}\right\} \tag{6}$$

where C_S is the surface concentration during hydrogen charging. Considering that no additional hydrogen was introduced during aging, this BC is reasonable. With the IC and BC in Eq. (6), the C_H profile during aging can also be obtained by solving Eq. (4). The numerical solution of Eq. (4) can be obtained via the simple explicit method described as

$$\left.\begin{array}{c} C_H(x_i, t_{a,n+1}) = C_H(x_i, t_{a,n}) + \frac{D_H \Delta t_a}{\Delta x^2}\left[C_H(x_{i+1}, t_{a,n}) - 2C_H(x_i, t_{a,n}) + C_H(x_{i-1}, t_{a,n})\right] \\ t_{a,n} = n \times \Delta t_a \\ x_i = i \times \Delta x \end{array}\right\} \tag{7}$$

where Δt_a and Δx are the increment (or step size) of aging time and depth, respectively. The superscript n and subscript i are the index of time steps and depth steps, respectively. To obtain the reasonable solution, the value of $\frac{D_H \Delta t_a}{\Delta x^2}$ was maintained below 0.5 according to the stability criterion for explicit method. Fig. 6b illustrates an example of calculation results of Eq. (7) for

$t_a = 50$ min. The figure shows the change in C_H that is divided by C_s as function of the distance from the surface. Two important features are noteworthy in Fig. 6b. First, the C_H/C_S profile under aging condition exhibits a peak (i.e., C_H reaches the maximum value at a certain depth from the surface) and a higher D_H value results in a larger peak-C_H depth at a given t_a. Second, the trend in Fig. 6b is somewhat similar to the ΔH_N profile shown in Fig. 2 (especially for SS316L, or Fig. 2d). Such overlap in the hardening profile and hydrogen content profile is reasonable, since the hydrogen-induced hardening is generally believed to follow solid solution strengthening mechanisms that is thus dependent on solute (hydrogen, in this case) concentration (Lee, 2014a; Zhao, 2017a, 2019). Based on these observations, we propose that the materials' D_H can be readily estimated by developing the mathematical relationship between the peak-ΔH_N depth and peak-C_H depth, and thereafter estimating the diffusion distance of hydrogen.

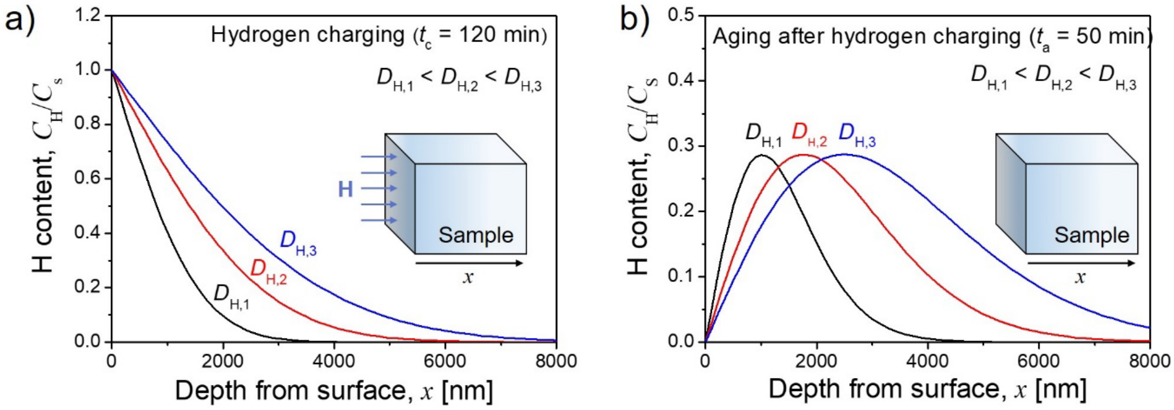

Fig. 6 Illustrations of the through-thickness districutions of hydrogen content under (a) hydrogen-charging and (b) aging after hydrogen-charging.

To start with, SS316L is taken as an example for the estimation. Note that the ΔH_N profile of SS316L shows a clear ΔH_N peak (Fig. 2d). Since the plastic zone radius (r_p) underneath the indentation is much larger than the indentation displacement (h), r_p should be considered instead of h for concisely estimating D_H (see Fig. 7a). According to Durst *et al.*

(2006), r_p can be expressed as:

$$r_p = f a_c \tag{8}$$

where a_c is contact radius and a constant f is typically determined as 2.2 for Berkovich indenter. The a_c can be converted from h using Oliver-Pharr method (Oliver and Pharr, 1992):

$$a_c = (h - \varepsilon \frac{P}{S}) \cot \beta \tag{9}$$

where $\varepsilon = 0.75$ (for Berkovich indenter) and S is the measured stiffness. β is the angle between sample surface and conical indenter, and the equivalent β for a three-sided pyramidal Berkovich indenter is 19.7° (Fischer-Cripps, 2011). Consequently, the values of r_p are thus estimated using Eqs. (8) and (9). With the obtained r_p value, nanohardness data shown in Fig. 2d is converted into ΔH_{N0} vs. r_p as shown in Fig. 7b. In contrast to Fig. 2d, ΔH_{N0} in Fig. 7b represents the difference in hardness between the short-term aged and long-term aged samples (i.e., $\Delta H_{N0} = H_{N,120CYA} - H_{N,120C2880A}$, where $Y \leq 130$) to exclude the potential effect, if any, of charging-induced microstructural change. The r_p showing the maximum ΔH_{N0} for the 120C50A, 120C90A, and 120C130A conditions are determined as 1144, 1517, and 1395 nm, respectively. Note that the experimental data in Fig. 7b were fitted by asymmetric double sigmoidal function to obtain the maximums in curves. To determine the D_H values for each case by solving Eq. (4), an arbitrary value of D_H was put into Eqs. (5)–(7). Then, it was varied until the peak depth in C_H profile became equal to the peak r_p in ΔH_{N0} profile, at which the corresponding D_H was determined as the D_H of each case. Fig. 7c shows an example of the effect of slightly varying D_H values on the hydrogen content profiles in 120C50A condition. As summarized in Fig. 7d, D_H estimated for the 120C50A, 120C90A, and 120C130A conditions are 1.25×10^{-16}, 1.45×10^{-16}, and 0.92×10^{-16} m^2/s, respectively. The averaged value over these three D_H values is ~1.21×10^{-16} m^2/s. It is noteworthy that hydrostatic stress field formed during nanoindentation may potentially redistribute hydrogen atoms in the vicinity of the indentation through stressdriven hydrogen diffusion. Nevertheless, in view of the relatively “high” strain rate (as compared to the low hydrogen diffusivity in FCC alloys) and the short time in indentation loading (~90 s), the hydrogen redistribution (by diffusion) would be rather limited. Additionally, the levels of stresses underneath a sharp indenter are independent of indentation displacement due to the so-called geometrical self-similarity of the sharp indenter. Therefore, the magnitude of hydrogen redistribution during nanoindentation remains almost constant with indentation displacement. As a result, its effect on the depth at which the maximum hydrogen concentration appears, if any, is negligible.

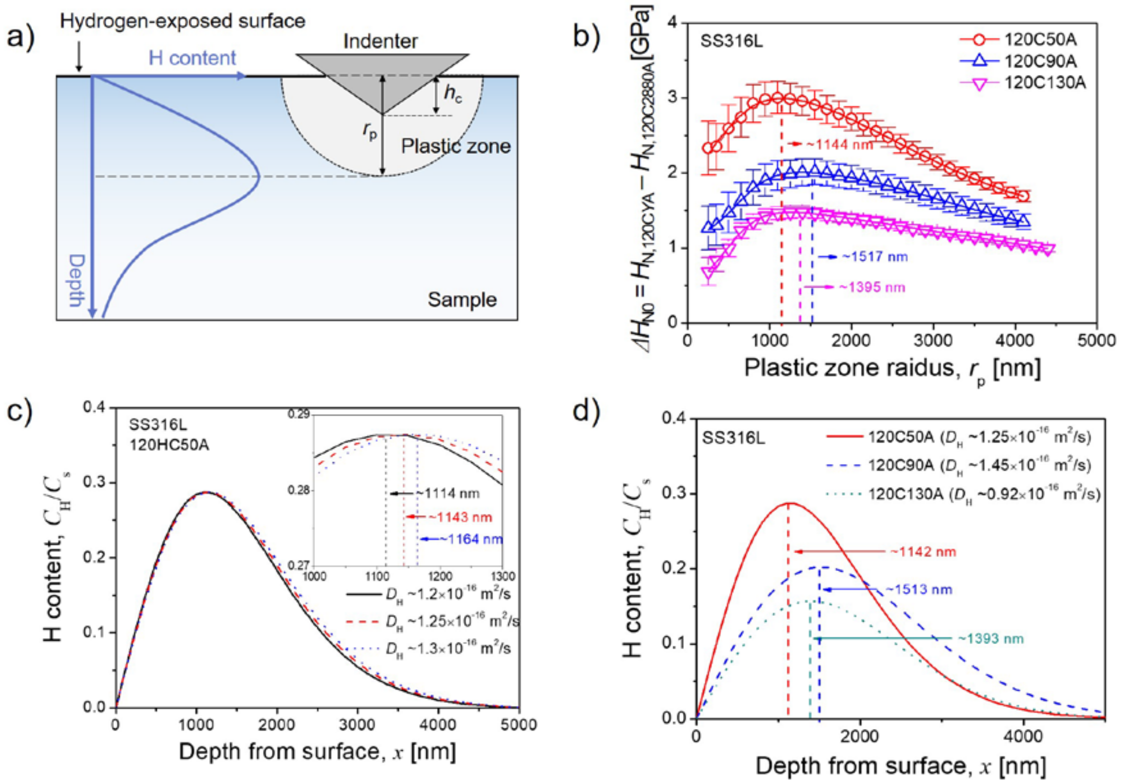

Fig. 7 (a) Schematic illustration showing through-thickness districutions of hydrogen content and plastic zone of the nanoindentation test; (b–d) an example presenting how to estimate hydrogen diffusivity and the obtained results for SS316L.

Based on the demonstration of the method in SS316L, an estimation of the D_H value in

CoCrNi MEA is also attempted hereafter using the same approach. It is noteworthy that, however, there is no clear ΔH_N peak observed within the current indentation depth range under the 120 min hydrogen charging, as shown in Fig. 2b. Since a visible ΔH_N peak is a necessity for applying our proposed methodology, a shorter hydrogen charging time of 30 min was attempted and then the nanoindentations with the same condition were conducted. Fig. 8a displays the variation of H_N vs. h in CoCrNi MEA. It is intriguing to note that hydrogen-induced softening-to-hardening transition with increasing h was observed for the short-term aging (i.e., $t_a \leq 130$ min), whereas hydrogen-induced softening prevailed at all h when t_a was prolonged to 2880 min. This is consistent with the results obtained from the 120 min hydrogen charging condition (Fig. 3a). As in the case of SS316L, ΔH_{N0} values were calculated as $H_{N,30CYA}$ – $H_{N,30C2880A}$ (where $Y \leq 130$ min) at the same h and provided as a function of h in Fig. 8b. With the ΔH_{N0} vs. h plot in Fig. 8b, ΔH_{N0} vs. r_p plot was obtained and displayed in Fig. 8c. For calculating r_p, $f = 2.2$ is adopted for the CoCrNi MEA. As shown in Fig. 8c, short-term hydrogen charging indeed leads to the appearance of ΔH_N peaks, enabling the estimation of D_H via the proposed method. The C_H profiles for the CoCrNi MEA obtained by Eqs. (5)–(7) are summarized in Fig. 8d; D_H values of the CoCrNi MEA estimated from the 30C50A, 30C90A, and 30C130A conditions are 2.88×10^{-16}, 1.85×10^{-16}, and 1.35×10^{-16} m^2/s, respectively. Thus, an averaged D_H value in the CoCrNi MEA is determined as ~2.03×10^{-16} m^2/s.

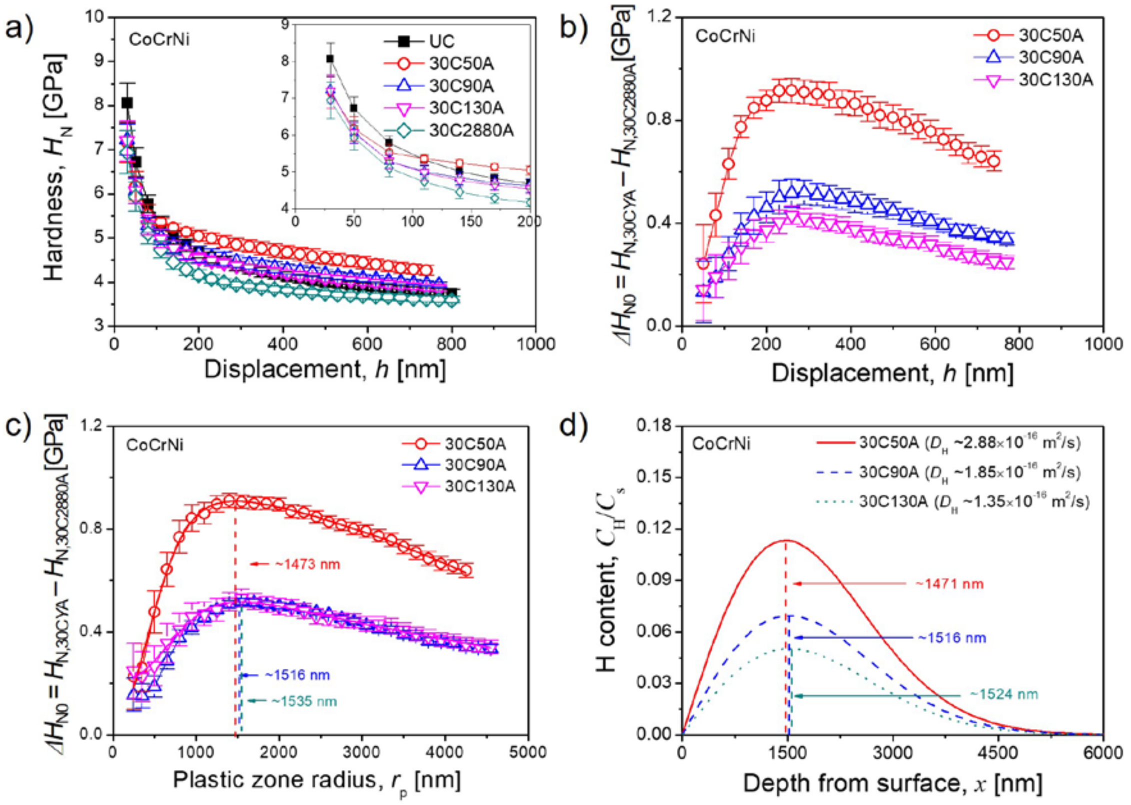

Fig. 8 An example presenting how to estimate hydrogen diffusivity and the obtained results for CoCrNi MEA. Note that ΔH_N values in (b,c) were calculated from the difference in H_N between the short-term aged and long-term aged samples; i.e., $\Delta H_N = H_{N,30CYA} - H_{N,30C2880A}$, where $Y \leq 130$ min.

5. Influences of hydrogen in CoCrNi *vs.* 316L

5.1 Hydrogen diffusivity and solubility

The nanoindentation analysis in Section 4.2 revealed that hydrogen diffusion in the CoCrNi MEA is ~0.68 times faster than that in the SS316L. Besides, TDS results in Fig. 5 showed that CoCrNi MEA exhibits lower E_a value and higher extent of aging-induced hydrogen desorption than SS316L. All of these results lead to the conclusion that CoCrNi MEA may exhibit higher hydrogen diffusivity than the SS316L. The consistency between nanoindentation and TDS results confirms the validity of the novel methodology proposed here. There exist, however, relatively large deviations in the D_H values estimated from our method for different aging times (Fig. 7d and 8d). It should be noted that the crystalline defects (e.g., dislocations, grain boundaries), which can affect the hydrogen diffusion by trapping hydrogen atoms, are not homogeneously distributed throughout the material. On this basis, hydrogen diffusion behavior may vary across different localized regions, leading to non-negligible deviations in D_{H} value, especially through nano-scale experiment. Furthermore, as depicted in Fig. 1, both SS316L and CoCrNi MEA fabricated by DED exhibit highly complex microstructures. This complexity also leads to significant inhomogeneity in hydrogen diffusion behavior for DED-fabricated alloys. Consequently, the resulting D_{H} values obtained from Figs. 7d and 8d exhibit a relatively large deviation due to the pronounced spatial variations in hydrogen diffusion behavior within the material rather than the uncertainty of the proposed methodology.

To address this concern and ensure the reliability of the proposed method, the same analysis was carried out additionally on the conventionally manufactured (CM) SS316L and CoCrNi MEA with minimized complexity. As shown in Figs. 9a and 9d, the microstructures of CM SS316L and CoCrNi consisted of equiaxed grains with an average grain size of ~63 μm and ~50 μm, respectively. The observed effects of hydrogen on H_{N} in the CM samples are consistent with those in the DED samples; i.e., only CM CoCrNi MEA showed the hydrogen-induced softening-to-hardening transition with increasing h (Fig. S2 in SI). Based on the ΔH_{N0} vs. r_p curves in Figs. 9b and 9e, the C_{H} profiles for the CM SS316L and CoCrNi MEA obtained by Eqs. (5)–(7) are plotted in Figs. 9c and 9f, respectively. The average D_{H} values for CM SS316L and CoCrNi MEA were ~2.19×10^{-16} m/s^2 and ~6.08×10^{-16} m/s^2, respectively. Although the D_{H} values in the CM samples are consistently higher than those in the DED counterparts, a similar conclusion can be drawn that D_{H} in CoCrNi MEA is higher than that in SS316L, regardless of the manufacturing method. Furthermore, both CM SS316L and CoCrNi MEA exhibited relatively small deviations in D_{H} values (Figs. 9c and 9f). Additionally, the estimated

D_H values for CM SS316L and CoCrNi MEA are well within the range reported in the literature (~1.40–5.00 × 10^{-16} m^2/s for austenitic stainless steels (Kishimoto, 1985; Lee, 2014b; Lin, 2020; Xiukui, 1989) and ~3.7×10^{-16} m^2/s for CoCrFeMnNi HEA (Marques, 2021)). All these results provide further support for the validity of the novel methodology.

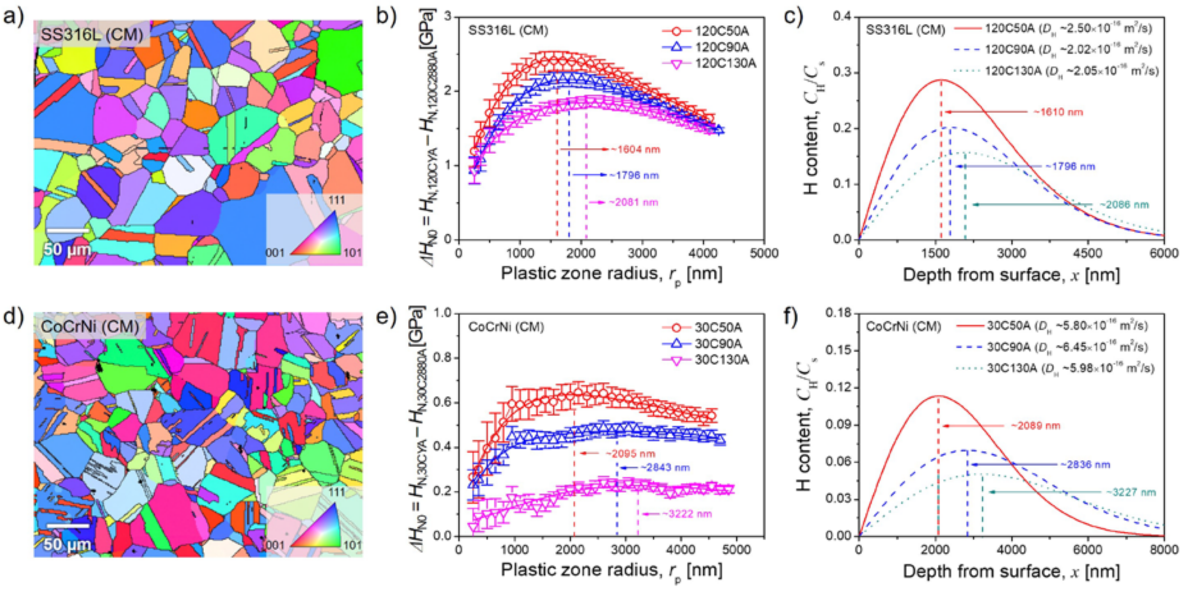

Fig. 9 Microstructure and nanoindentation analysis on hydrogen diffusivity for the conventionally manufactured (CM) (a–c) SS316L and (d–f) CoCrNi MEA.

Considering that CM SS316L and CoCrNi MEA exhibit similar microstructure (see Figs. 9a and 9c), the enhanced hydrogen diffusivity in CoCrNi MEA might be attributed to its intrinsic features such as chemical composition and the interaction between hydrogen and the trapping sites. Recently, it has been reported that the hydrogen diffusivity in FCC alloys could be enhanced with increasing Ni content, but could be retarded by increasing Cr content (Marques, 2021). Additionally, Zhou *et al.* (2022) explored the hydrogen diffusivity the H/MEAs through kinetic Monte Carlo simulations combined with DFT calculation, and proposed a quantitative relationship between the hydrogen diffusivity (at RT) and chemical composition described as:

$$\log(D_H) = 0.096Fe - 0.47Co + 3.05Ni - 1.01Cr - 1.66Mn - 15.05 \quad (10)$$

where Fe, Co, Ni, Cr, and Mn represent the atomic percentage of each element. On this basis, it can be suggested that the increased Co, Cr, and Mn content can reduce the hydrogen diffusivity coefficient whereas an increase of Fe and Ni would result in the opposite effect. Compared to SS316L, CoCrNi alloy has higher concentrations of Co and Cr, which have a retarding effect on D_H. Conversely, CoCrNi alloy also contains higher concentration of Ni, which enhance D_H. To consider the influence of all these elements, the D_H values in SS316L and CoCrNi alloys were also calculated using Eq. (10), from which ~1.63×10^{-15} and ~3.15×10^{-15} m/s^2 were obtained respectively. Although these values seem to be overestimated, this calculation supports the conclusion that the higher D_H in the CoCrNi alloy, in comparison to SS316L, is mainly attributed to its higher Ni content. To gain further insights on the relationship between D_H and the constituent elements, the variations in D_H values as a function of the content of elements are plotted in Fig. 10. For comparison purposes, D_H values for various FCC metals and alloys (including austenitic stainless steels (Kishimoto, 1985; Lee, 2014b; Lin, 2020; Qu, 2019; Tsong-Pyng and Altstetter, 1986; Xiukui, 1989), CoCrFeMnNi HEA (Marques, 2021), Ni-based superalloys (Kishimoto, 1985; Uhlemann and Pound, 1998)), and pure Ni (Arantes, 1993; Brass and Chanfreau, 1996; Kuhn and Johnson, 1991) are also provided in Fig. 10. The figure also includes the D_H values obtained using Eq. (10) for the present SS316L and CoCrNi MEA. The diffusion parameters for those alloys are summarized in Table 2. It is noteworthy that only gaseous hydrogen permeation results were chosen for the literature data, since D_H values at RT obtained from the electrochemical hydrogen permeation are typically larger than those extrapolated from gaseous hydrogen permeation results (Lee, 2020; Lin, 2020). The reason for such discrepancy lies in the fact that D_H obtained from gaseous hydrogen permeation test at high temperature is closer to pure lattice diffusion. However, at RT, hydrogen diffusion in the bulk material is a result of the mixture of hydrogen diffusion through the lattice and grain boundary (Lin, 2020; Oudriss, 2012). This may lead to an overestimation of D_H value at RT obtained from electrochemical hydrogen permeation test due to the contribution of hydrogen diffusion through grain boundary. On the other hand, our method estimates D_H values using nanoindentation, where the size of plastic zone induced by nanoindentation (~4.5 μm) is much smaller than the grain sizes (~270–480 μm for DED samples and ~50 μm for CM samples). Therefore, the D_H values obtained via the proposed method may align more closely with the results of pure lattice diffusion and reflect the intrinsic property of the alloy. Given these considerations, it is reasonable to compare our results to gaseous hydrogen permeation results rather than electrochemical permeation results. It can be seen in Fig. 10 that D_H values in M/HEAs are relatively higher than those in the austenitic steels, but much lower than those in the pure Ni. Similar conclusion has been reached by Lee *et al.* (2020) that hydrogen diffusivity is only marginally higher in CoCrFeMnNi HEA than in SS316L. The more noteworthy result in Fig. 10 is that the D_H in FCC metals and alloys tends to increase with Ni content. On this basis, the higher Ni content in the CoCrNi MEA (~35.7 wt%) than SS316L (~13.8 wt%) might be the reason why the former has higher D_H. In contrast to Ni, no clear trend is found for other elements. Especially, for varying Cr, Mn, and Co, the D_H values are distributed over a very wide range at the given concentration (see the regions displayed with red rectangle in Fig. 10). This suggests that Ni content plays the predominant role in in determining the hydrogen diffusivity in FCC alloys among the constituent elements.

The increase in D_H with Ni content has indeed been reported in other FCC alloys such as Ni-based superalloys (Uhlemann and Pound, 1998) and binary Fe-Ni alloys (Beck, 1971). Alloys with a high Ni content have only a small number of unfilled 3*d* electron states to hold the 1s electron from hydrogen (Uhlemann and Pound, 1998). As a result, the influence of *d*-vacancies on the cohesive force between metal atoms and hydrogen is too weak to trap hydrogen atoms at the lattice sites, leading to low hydrogen solubility yet high hydrogen diffusivity. This was supported by the fact that hydrogen-induced lattice dilation became less pronounced with increasing Ni content (Uhlemann and Pound, 1998). A decrease in hydrogen-induced lattice dilation reflects a decrease in the ability to trap hydrogen and, consequently, an increase in hydrogen diffusivity.

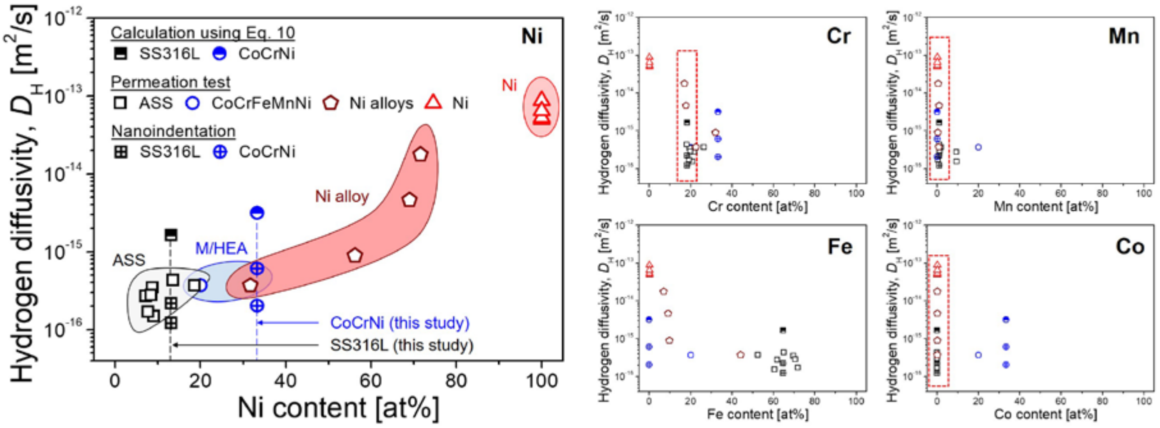

Fig 10. The variations in hydrogen diffusivity (at RT) with the concentration of elements for FCC metals and alloys, including austentic stainless steels (Kishimoto, 1985; Lee, 2014b; Lin, 2020; Qu, 2019; Tsong-Pyng and Altstetter, 1986; Xiukui, 1989), M/HEAs (Marques, 2021), Ni alloys (Kishimoto, 1985; Uhlemann and Pound, 1998), and pure Ni (Arantes, 1993; Brass and Chanfreau, 1996; Kuhn and Johnson, 1991).

Table 2. Hydrogen diffusivity, D_H, in various FCC metals and alloys. D_H follows the Arrhenius relation, $D_H = D_0 exp(-E_d/RT)$, where D_0 is a pre-exponent coefficient, E_d is the activation barrier energy for diffusion, R is the universal gas constant (8.314 J·mol^{-1}K^{-1}), and T is the absolute temperature. Note that the values marked with * are for the additively manufactured alloy and the others are for the conventionally manufactured one. (ASS: Austenitic stainless steel)

Materials	D_0 [m^2/s]	E_d [kJ/mol]	D_H @ RT [m^2/s]	Refs.
SS316	1.24×10^{-6}	55.10	2.7×10^{-16}	(Lee, 2014b)
	1.30×10^{-6}	54.03	4.4×10^{-16}	(Kishimoto, 1985)

	*1.01×10^{-6}	*56.16	*1.4×10^{-16}	(Lin, 2020)
	4.79×10^{-7}	51.6	4.3×10^{-16}	(Xiukui, 1989)
	-	-	*1.2×10^{-16}	This study
	-	-	2.2×10^{-16}	This study
SS304	8.90×10^{-7}	53.9	3.2×10^{-16}	(Qu, 2019)
	7.69×10^{-7}	53.3	3.5×10^{-16}	(Tsong-Pyng and Altstetter, 1986)
	6.43×10^{-7}	53.4	2.8×10^{-16}	(Xiukui, 1989)
Other ASSs	1.30×10^{-7}	55.0	3.0×10^{-17}	(Tsong-Pyng and Altstetter, 1986)
	7.16×10^{-7}	53.0	3.7×10^{-16}	(Tsong-Pyng and Altstetter, 1986)
	2.49×10^{-7}	51.2	2.7×10^{-16}	(Xiukui, 1989)
	6.33×10^{-7}	55.0	1.5×10^{-16}	(Xiukui, 1989)
	4.61×10^{-7}	53.8	1.7×10^{-16}	(Xiukui, 1989)
CoCrFeMnNi	4.30×10^{-7}	51.7	3.7×10^{-16}	(Marques, 2021)
CoCrNi	-	-	*2.0×10^{-16}	This study
	-	-	6.1×10^{-16}	This study
Alloy 600	3.41×10^{-7}	44.9	4.6×10^{-15}	(Uhlemann and Pound, 1998)
	4.90×10^{-7}	42.5	1.8×10^{-14}	(Kishimoto, 1985)
Alloy 690	6.87×10^{-7}	50.7	8.9×10^{-16}	(Uhlemann and Pound, 1998)
Alloy 800	5.41×10^{-6}	58.0	3.7×10^{-16}	(Uhlemann and Pound, 1998)
Ni	3.60×10^{-7}	37.7	8.8×10^{-14}	(Kuhn and Johnson, 1991)
	1.10×10^{-6}	41.6	5.0×10^{-14}	(Arantes, 1993)
	6.60×10^{-7}	40.5	5.3×10^{-14}	(Arantes, 1993)
	1.90×10^{-7}	36.9	6.5×10^{-14}	(Brass and Chanfreau, 1996)

To ascertain whether the scenario described above could be extended to the present alloys, the hydrogen solution energy, $E_{\text{H-sol}}$, at the interstitial sites was investigated via DFT calculation. Taking the diversity of chemical environments in the alloys into consideration, nearly ten random interstitial sites were chosen, including octahedral interstitial (OI) sites and tetrahedral interstitial (TI) sites, and then $E_{\text{H-sol}}$ at each site were calculated using Eq. (1). Fig. 11a shows the distribution of $E_{\text{H-sol}}$ value in CoCrNi MEA and SS316L in which each OI or TI position was numbered as OI1, OI2, and so on. Consistent with previous research (Marques, 2021; Ren, 2019; Zhou, 2022), it is evident that $E_{\text{H-sol}}$ varies with the local chemical environment, and hydrogen atoms tend to reside in octahedral sites rather than in tetrahedral sites for both CoCrNi MEA and SS316L. More importantly, as shown in Fig. 11a, the CoCrNi MEA exhibits higher average $E_{\text{H-sol}}$ in octahedral sites (0.18 eV), compared to the SS316L (−0.53 eV), which suggests that the SS316L can trap hydrogen more efficiently and hence show slower hydrogen diffusivity than the CoCrNi MEA. The influence of Ni concentration on $E_{\text{H-sol}}$ could be further supported by the results that $E_{\text{H-sol}}$ tends to increase with the number of Ni atom around the OI site for both CoCrNi and SS316L (Fig. 11b). For instance, for CoCrNi, OI2 and OI3 sites having 2 neighboring Ni atoms show higher solution energies than OI1 and OI4 having only 1 Ni atom. This observation suggests that the concentration and arrangement of Ni atoms play a significant role in determining the hydrogen solution energy. Therefore, it can be concluded that the high Ni content in the CoCrNi MEA indeed reduces the ability to trap hydrogen and thus increases hydrogen diffusivity.

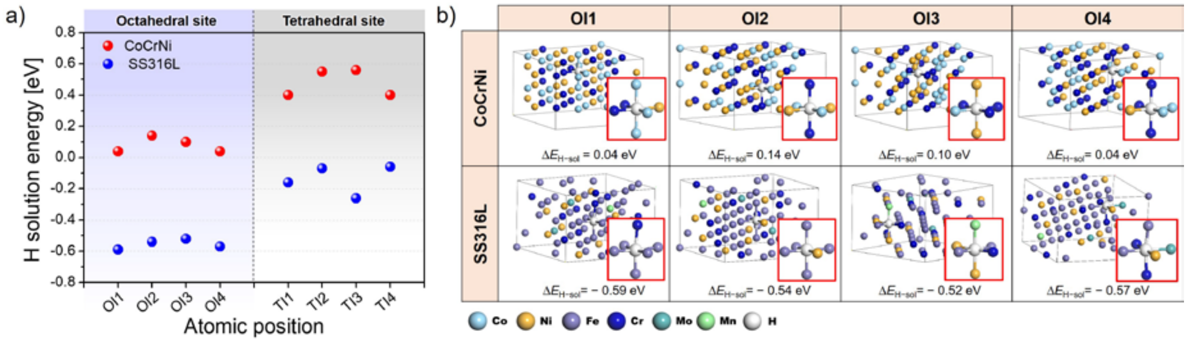

Fig. 11 (a) Variations in hydrogen solution energies at differenct types of octahaedral interstitial (OI) and tetrahedral interstitial (TI) sites. (b) Schematic illustrations of the OI sites along with their corresponding hydrogen solution energies.

It is noteworthy here that the relatively lower D_H values were observed in DED samples compared to CM samples, for both SS316L and CoCrNi MEA. In contrast to CM samples, DED samples contain a high density of dislocations along with the large fraction of solidification cellular substructure (as shown in Fig. 1). Such a unique microstructural feature in DED alloys may lead to degradation of hydrogen diffusion by providing high fraction of crystalline defects. In fact, the effect of complex microstructure in AM alloys on hydrogen diffusivity is still controversial. While AM-induced complex microstructure was reported to decrease the hydrogen diffusion in SS316L (Park, 2021) and CoCrFeMnNi HEA (Lin, 2022), the possibility that the sub-grain boundary can act as rapid diffusion channel for hydrogen atom in AM-fabricated SS316L was also addressed (Lin, 2020). Therefore, additional systematic experiments and simulations on various FCC alloys are required to confirm the exact role of AM-induce complex microstructure in affecting hydrogen diffusion.

On the other hand, one may wonder why CoCrNi MEA and SS316L have comparable hydrogen content (according to TDS data in Fig. 5) despite the fact that CoCrNi MEA exhibits an inferior ability to trap hydrogen. Regarding this, it should be noted that hydrogen content measured by TDS is the total hydrogen amount in the sample's whole volume. Since CoCrNi MEA and SS316L have different hydrogen permeation depths (or volumes) due to their dissimilar D_H, the comparable "total" hydrogen content (i.e., hydrogen content measured by TDS) may result in distinct "local" hydrogen contents between the alloys. In order to assess the genuine hydrogen trap ability, it is necessary to investigate the difference in "local" hydrogen content. According to Pontini and Hermida (1997), the local hydrogen concentration at the "surface" C_S, can be determined as

$$C_S = \frac{w \cdot C_M}{4} \sqrt{\frac{\pi}{D_H t_c}} \tag{10}$$

where w is sample thickness (~1 mm) and C_M is the mean hydrogen content in the sample (viz. ~9.3 wt. ppm for CoCrNi MEA and ~7.9 wt. ppm for SS316L). By using the D_H values obtained from nanoindentation (*viz.* ~2.03×10^{-16} m^2/s for CoCrNi MEA and ~1.21×10^{-16} m^2/s for SS316L), C_s were estimated to be ~3408 wt. ppm for CoCrNi MEA and ~3750 wt. ppm for SS316L. Assuming that the surface is saturated with hydrogen during electrochemical charging, these values demonstrate that CoCrNi MEA indeed has a lower hydrogen trapping capacity than SS316L.

5.2. Hydrogen effects on nanohardness

As shown in the Section 3.2, a competition between hydrogen-induced hardening and softening could occur in CoCrNi MEA, whereas only hydrogen-induced hardening prevails in

SS316L. Hydrogen-induced hardening has been widely reported in the FCC alloys including conventional austenitic steels (Han, 2014; Nibur 2006) and H/MEAs (Soundararajan, 2020; Zhao, 2017a, 2017b) and usually attributed to the simple solid solution hardening (such as dislocation dragging or pinning) (Barnoush al., 2012; Lee, 2014a) or reduction in stacking fault energy (SFE) (Wen, 2004). Such SFE reduction induced by interstitial elements such as C, N, and H (that is referred to as "Suzuki effect" (Dieter, 1989)) causes the limited activity of cross-slip and thus achieves a certain amount of strengthening (Nibur, 2006). On the other hand, a few nanoindentation studies have reported the hydrogen-induced softening (Lee, 2014a; Zhao, 2015, 2016, 2017a). Although the detailed mechanism for hydrogen-induced softening is not fully understood at this point, two possible scenarios have been suggested; the first one is "hydrogen-assisted dislocation motion" and the other is "hydrogen-induced excess vacancies". For the first one, the hydrogen trapped at dislocations enhances the dislocations' mobility either through modifying the Peierls potential of screw dislocations (Matsui, 1979) or through hydrogen's elastic shielding effect on the interactions between dislocations (Birnbaum and Sofronis, 1994). However, we can exclude this scenario for the present case, since the CoCrNi MEA exhibits hydrogen-induced softening only at the shallow indentation depth ($h < 150$ nm) or after long-term aging ($t_a > 24$ h) in which most of the hydrogen atoms were already desorbed from the trapping sites including dislocations. Therefore, in the present study, the second scenario is a more reasonable one. It has been proposed that the attraction between interstitial hydrogen and vacancy results in a higher equilibrium vacancy concentration in hydrogen-charged alloys than in uncharged ones, as the formation energy of vacancy is decreased by the presence of hydrogen atoms (Carr and McLellan, 2004; Nazarov, 2010). Such hydrogen-induced excess vacancies can result in the formation of voids and bubbles, which leads to non-negligible softening (Li, 2015; Zhao, 2016, 2017a).

On this basis, possible reasons for the transition from hydrogen-induced hardening to softening observed in the CoCrNi MEA upon RT aging are the following. During hydrogen-charging, hydrogen atoms reside at the lattice (and/or other trapping sites) and some excessive vacancies are formed at the same time. Therefore, a competition between hardening (by solid solution strengthening of hydrogen) and softening (by vacancies) may occur. Right after hydrogen-charging, hydrogen-induced hardening is predominant due to the high hydrogen concentration. Upon aging at RT, however, the solid solution strengthening of hydrogen continuously decreases due to hydrogen outgassing. Nevertheless, since the lattice diffusion of constituent elements is extremely low at room temperature (e.g., diffusivity of Ni in CoCrFeMnNi HEA is ~4.36×10^{-59} m^2/s (Tsai, 2013)), the excessive vacancies formed during hydrogen-charging might not be recovered during RT aging and thus the contribution of the excessive vacancies to softening remains invariant. Eventually, after long-term aging, most hydrogen desorbs out of the specimen and the softening effect of vacancies becomes predominant. The transition from hydrogen-induced softening to hardening with increasing indentation depth shown in Fig. 2b can be explained in a similar manner. On the other hand, only hydrogen-induced hardening is predominant in the SS316L; the extent of hydrogen-induced hardening decreases with aging time, but softening does not occur even after the prolonged aging (~1440 min). Based on the above concept, it is reasonable to expect that the hydrogen-charging on SS316L has negligible effect of vacancy concentration and thus only solid solution hardening of hydrogen prevails.

To clarify how the interstitial hydrogen affects the vacancy (defect) formation, we performed DFT calculations to estimate the vacancy formation energy, ΔE_{vac}, (refer to Eq. (2) for the exact formula), which measures the strength of the interatomic cohesion in the matrix. The ΔE_{vac} values calculated with the CoCrNi MEA and SS316L models are displayed in Fig. 12. Although the interstitial hydrogen atom indeed reduces the ΔE_{vac} of CoCrNi MEA from an average of 2.00 eV to 1.39 eV (Figs. 12a and 12b), the ΔE_{vac} of SS316L oppositely responses to the interstitial hydrogen as it increases by 55% (from 1.07 eV to 1.66 eV, Figs. 12c and 12d) upon introduction of hydrogen into the matrix. These results suggest that hydrogen facilitates vacancy formation and thus increases the vacancy concentration in the CoCrNi MEA, but instead, strengthens the interatomic cohesion in the SS316L. Therefore, we can conclude that the hydrogen-induced softening observed in the CoCrNi MEA is mainly attributed to the "superabundant vacancies" formation. By contrast, the SS316L is not feasible to form "superabundant vacancies" under the hydrogen environment and thus only exhibits hydrogen-induced hardening.

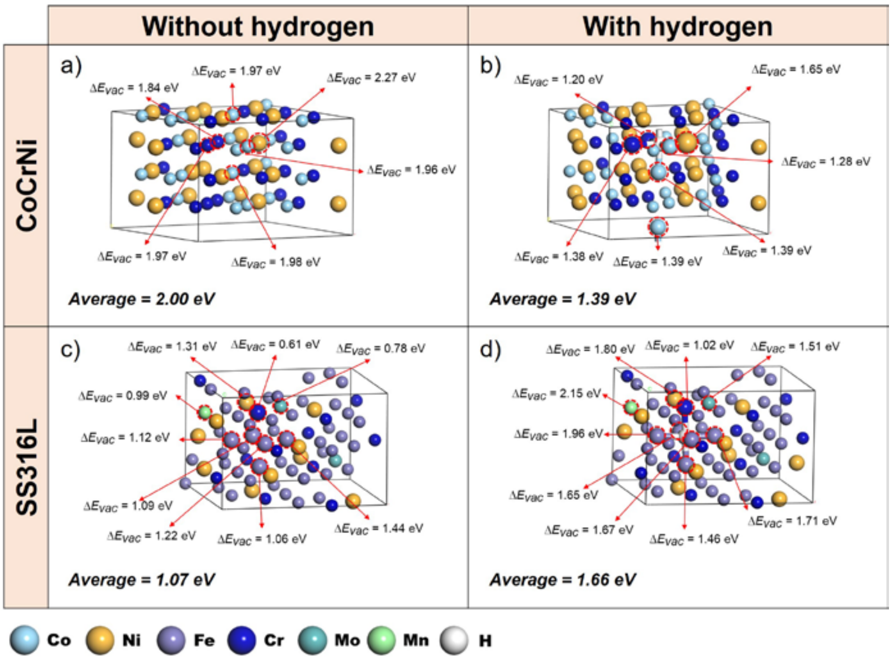

Fig. 12 DFT-calculated average vacancy formation energy, ΔE_{vac}, with and without hydrogen interstitial. (a,b) CoCrNi MEA and (c,d) SS316L. Each red arrow indicates the location of the original matrix atom used for ΔE_{vac} calculation. The ΔE_{vac} values calculated over six (CoCrNi) or nine (SS316L) sites were averaged and used for evaluating the effect of hydrogen on the ΔE_{vac}.

5. Conclusions and outlook

In the present study, we suggested a novel approach to estimate hydrogen diffusivity in FCC alloys by means of nanoindentation experiments and analysis. The following are the key conclusions of this investigation.

1. In consideration of the plastic zone size around the indentation, the relationship between hydrogen-induced change in nanoindentation hardness (ΔH_N) and the depth from the sample surface was established for the sample subjected to hydrogen charging and subsequent aging. Since the through-thickness distribution of hydrogen concentration (C_H) under the identical condition can be readily calculated by solving Fick's law, hydrogen diffusivity can thus be determined by correlating the peak-ΔH_N depth with the peak-C_H depth.
2. The hydrogen diffusivity values of SS316L and CoCrNi MEA fabricated by direct energy deposition (DED) and conventional manufacturing (CM) were estimated by such novel methodology, and it was revealed that hydrogen diffusivity at RT in CoCrNi MEA was higher than that in SS316L, regardless of the manufacturing method. Especially, the estimated hydrogen diffusivity for CM SS316L and CoCrNi MEA were in good agreement with the literature data, validating the appropriateness of the proposed novel methdology.
3. The enhanced hydrogen diffusivity in CoCrNi MEA can be rationalized in consideration of an inferior ability to trap hydrogen, which can be supported by the DFT calculation of hydrogen solution energy.
4. The D_H values in the DED samples were relatively lower than those in the CM samples for both SS316L and CoCrNi MEA, suggesting that the solidification cellular substructure along with high-density dislocations may play a critical role in impeding hydrogen diffusion in FCC alloys.
5. While only hydrogen-induced hardening, which is due to solid solution

strengthening, prevailed in SS316L, CoCrNi MEA exhibited a competition between hydrogen-induced hardening and softening; softening dominated hardening behavior when most of hydrogen atoms were desorbed from the sample. Through the DFT calculation on vacancy formation energy, this softening was attributed to “superabundant vacancies” formation caused by hydrogen. By contrast, the SS316L is not feasible to form “superabundant vacancies” under the hydrogen environment and thus only exhibits hydrogen-induced hardening.

Before closing, it would be constructive to briefly discuss the advantages and disadvantages of our novel methodology for estimating hydrogen diffusivity compared to the traditional hydrogen permeation experiments. The main advantage of our method is that it does not require preparation of extremely thin sample and is hence time-saving compared to traditional permeation tests. As a result, this method is appropriate for evaluating hydrogen diffusivity at RT for FCC alloys where hydrogen permeation is even more difficult and time consuming. Additionally, the use of nanoindentation experiments makes it possible to understand the plastic deformation behavior and estimate hydrogen diffusivity simultaneously. The small-volume detection capability of nanoindentation also enables the estimation of hydrogen diffusivity for specific microstructures, such as grain interior, grain/twin boundary, and constituent phases in multi-phase alloys. Despite the above advantages, however, it is also important to acknowledge the stochastic nature of the mechanical responses measured on small-volume samples, which necessitates more repeated indentation tests to obtain statistically reliable data. In addition, for BCC materials with relatively high hydrogen diffusivity even at RT, a clear ΔH_N-peak may be absent within the displacement range that nanoindentation can cover, making the method challenging to apply. In such cases, however, hydrogen diffusivity measurement via traditional permeation test is relatively easy to conduct and analyze at both RT and the elevated temperature. In a nutshell, our novel methodology is specifically proposed as an alternative technique for FCC alloys, which present challenges when subjected to traditional permeation tests due to the intrinsically low hydrogen diffusivity in them.

Acknowledgements

The work at Chungnam National University was supported by the National Research Foundation (NRF) grant funded by the Korean government (MSIT) (No. 2021R1A4A1031494 and No. 2021R1F1A1048393). YZ would like to thank the support by Agency for Science, Technology and Research (A*STAR) of Singapore via the Structural Metal Alloys Programme (No. A18B1b0061).

References

Abdolvand, H., 2019. Progressive modelling and experimentation of hydrogen diffusion and precipitation in anisotropic polycrystals. Int. J. Plast. 116, 39–61. https://doi.org/10.1016/J.IJPLAS.2018.12.005

An, D., Krieger, W., Zaefferer, S., 2020. Unravelling the effect of hydrogen on microstructure evolution under low-cycle fatigue in a high-manganese austenitic TWIP steel. Int. J. Plast. 126, 102625. https://doi.org/10.1016/j.ijplas.2019.11.004

Arantes, D.R., Huang, X.Y., Marte, C., Kirchheim, R., 1993. Hydrogen diffusion and permeation in micro- and nanocrystalline nickel. Acta Metall. Mater. 41, 3215–3222. https://doi.org/10.1016/0956-7151(93)90051-S

Barnoush, A., Asgari, M., Johnsen, R., 2012. Resolving the hydrogen effect on dislocation nucleation and mobility by electrochemical nanoindentation. Scr. Mater. 66, 414–417. https://doi.org/10.1016/j.scriptamat.2011.12.004

Beck, W., Bockris, J.O.M., Genshaw, M.A., Subramanyan, P.K., 1971. Diffusivity and solubility of hydrogen as a function of composition in Fe-Ni alloys. Metall. Trans. 2, 883–888. https://doi.org/10.1007/BF02662750

Birnbaum, H.K., Sofronis, P., 1994. Hydrogen-enhanced localized plasticity—a mechanism for hydrogen-related fracture. Mater. Sci. Eng. A 176, 191–202. https://doi.org/10.1016/0921-5093(94)90975-X

Blöchl, P.E., 1994. Projector augmented-wave method. Phys. Rev. B 50, 17953–17979. https://doi.org/10.1103/PhysRevB.50.17953

Brass, A.M., Chanfreau, A., 1996. Accelerated diffusion of hydrogen along grain boundaries in nickel. Acta Mater. 44, 3823–3831. https://doi.org/10.1016/1359-6454(95)00446-7

Carr, N.Z., McLellan, R.B., 2004. The thermodynamic and kinetic behavior of metal–vacancy–hydrogen systems. Acta Mater. 52, 3273–3293. https://doi.org/10.1016/j.actamat.2004.03.024

Chandan, A.K., Kishore, K., Hung, P.T., Ghosh, M., Chowdhury, S.G., Kawasaki, M., Gubicza, J., 2022. Effect of nickel addition on enhancing nano-structuring and suppressing TRIP effect in Fe40Mn40Co10Cr10 high entropy alloy during high-pressure torsion. Int. J. Plast. 150. https://doi.org/10.1016/j.ijplas.2021.103193

Cullen, D.A., Neyerlin, K.C., Ahluwalia, R.K., Mukundan, R., More, K.L., Borup, R.L., Weber, A.Z., Myers, D.J., Kusoglu, A., 2021. New roads and challenges for fuel cells in heavy-duty transportation. Nat. Energy 6, 462–474. https://doi.org/10.1038/s41560-021-00775-z

Deng, Y., Barnoush, A., 2018. Hydrogen embrittlement revealed via novel in situ fracture experiments using notched micro-cantilever specimens. Acta Mater. 142, 236–247. https://doi.org/10.1016/j.actamat.2017.09.057

Dieter, G.E., 1989. Mechanical metallurgy., Mechanical metallurgy. McGraw-Hill, New York,. https://doi.org/10.5962/bhl.title.35895

Durst, K., Backes, B., Franke, O., Göken, M., 2006. Indentation size effect in metallic materials: Modeling strength from pop-in to macroscopic hardness using geometrically necessary dislocations. Acta Mater. 54, 2547–2555. https://doi.org/10.1016/J.ACTAMAT.2006.01.036

Ebner, A.S., Plesiutschnig, E., Clemens, H., Pippan, R., Maier-Kiener, V., 2021. Rate-depending plastic deformation behaviour in a nickel-base alloy under hydrogen influence. Int. J. Hydrogen Energy 46, 38132–38143. https://doi.org/10.1016/J.IJHYDENE.2021.09.030

Fischer-Cripps, A.C., 2011. Nanoindentation, 3rd ed., Springer, New York.

Gao, Z., Zhao, Y., Park, J.-M., Jeon, A.-H., Murakami, K., Komazaki, S., Tsuchiya, K., Ramamurty, U., Jang, J., 2022. Decoupling the roles of constituent phases in the strengthening of hydrogenated nanocrystalline dual-phase high-entropy alloys. Scr. Mater. 210, 114472. https://doi.org/10.1016/j.scriptamat.2021.114472

Gludovatz, B., Hohenwarter, A., Catoor, D., Chang, E.H., George, E.P., Ritchie, R.O., 2014. A fracture-resistant high-entropy alloy for cryogenic applications. Science (80-.). 345, 1153–1158. https://doi.org/10.1126/science.1254581

Gludovatz, B., Hohenwarter, A., Thurston, K.V.S., Bei, H., Wu, Z., George, E.P., Ritchie, R.O., 2016. Exceptional damage-tolerance of a medium-entropy alloy CrCoNi at cryogenic temperatures. Nat. Commun. 7, 10602. https://doi.org/10.1038/ncomms10602

Han, D.K., Kim, Y.M., Han, H.N., Bhadeshia, H.K.D.H., Suh, D.-W., 2014. Hydrogen and aluminium in high-manganese twinning-induced plasticity steel. Scr. Mater. 80, 9–12. https://doi.org/10.1016/j.scriptamat.2014.01.039

Henkelman, G., Jónsson, H., 2000. Improved tangent estimate in the nudged elastic band method for finding minimum energy paths and saddle points. J. Chem. Phys. 113, 9978–9985. https://doi.org/10.1063/1.1323224

Henkelman, G., Uberuaga, B.P., Jónsson, H., 2000. A climbing image nudged elastic band method for finding saddle points and minimum energy paths. J. Chem. Phys. 113, 9901–9904.

https://doi.org/10.1063/1.1329672

Hong, Y., Zhou, C., Zheng, Y., Zhang, L., Zheng, J., Chen, X., 2019a. Dependence of strain rate on hydrogen-induced hardening of austenitic stainless steel investigated by nanoindentation. Int. J. Hydrogen Energy 44, 14055–14063. https://doi.org/10.1016/J.IJHYDENE.2019.03.250

Hong, Y., Zhou, C., Zheng, Y., Zhang, L., Zheng, J., Chen, X., 2019b. Effect of hydrogen and strain rate on nanoindentation creep of austenitic stainless steel. Int. J. Hydrogen Energy 44, 1253–1262. https://doi.org/10.1016/J.IJHYDENE.2018.11.017

Isfandbod, M., Martínez-Pañeda, E., 2021. A mechanism-based multi-trap phase field model for hydrogen assisted fracture. Int. J. Plast. 144, 103044. https://doi.org/10.1016/j.ijplas.2021.103044

Kim, J., Tasan, C.C., 2019. Microstructural and micro-mechanical characterization during hydrogen charging: An in situ scanning electron microscopy study. Int. J. Hydrogen Energy 44, 6333–6343. https://doi.org/10.1016/j.ijhydene.2018.10.128

Kim, Y.S., Chae, H., Woo, W., Kim, D.-K., Lee, D.-H., Harjo, S., Kawasaki, T., Lee, S.Y., 2021. Multiple deformation scheme in direct energy deposited CoCrNi medium entropy alloy at 210K. Mater. Sci. Eng. A 828, 142059. https://doi.org/10.1016/j.msea.2021.142059

Kishimoto, N., Tanabe, T., Suzuki, T., Yoshida, H., 1985. Hydrogen diffusion and solution at high temperatures in 316L stainless steel and nickel-base heat-resistant alloys. J. Nucl. Mater. 127, 1–9. https://doi.org/10.1016/0022-3115(85)90056-X

Kissinger, H.E., 1957. Reaction Kinetics in Differential Thermal Analysis. Anal. Chem. 29, 1702–1706. https://doi.org/10.1021/ac60131a045

Kratzer, P., Neugebauer, J., 2019. The Basics of Electronic Structure Theory for Periodic Systems. Front. Chem. 7, 1–18. https://doi.org/10.3389/fchem.2019.00106

Kresse, G., Furthmüller, J., 1996. Efficient iterative schemes for ab initio total-energy calculations using a plane-wave basis set. Phys. Rev. B 54, 11169–11186. https://doi.org/10.1103/PhysRevB.54.11169

Kresse, G., Joubert, D., 1999. From ultrasoft pseudopotentials to the projector augmented-wave method. Phys. Rev. B 59, 1758–1775. https://doi.org/10.1103/PhysRevB.59.1758

Kuhn, D.K., Johnson, H.H., 1991. Transient analysis of hydrogen permeation through nickel membranes. Acta Metall. Mater. 39, 2901–2908. https://doi.org/10.1016/0956-7151(91)90106-B

Lee, D.-H., Jung, J.Y., Lee, K.H., Lee, S.Y., Zhao, Y., Lau, K.B., Wang, P., Ramamurty, U., 2023. Distinct effects of in-situ and ex-situ hydrogen charging methods on the mechanical behavior of CoCrFeNi high-entropy alloy fabricated by laser-powder bed fusion. J. Alloys Compd. 940, 168858. https://doi.org/10.1016/j.jallcom.2023.168858

Lee, D.-H., Zhao, Y., Lee, S.Y., Ponge, D., Jägle, E.A., 2022a. Hydrogen-assisted failure in Inconel 718 fabricated by laser powder bed fusion: The role of solidification substructure in the embrittlement. Scr. Mater. 207, 114308. https://doi.org/10.1016/j.scriptamat.2021.114308

Lee, D.-H., Gao, Z., Park, J.-M., Zhao, Y., Suh, J.-Y., Jägle, E.A., Tsuchiya, K., Ramamurty, U., Jang, J., 2022b. Nanomechanical and microstructural characterization on the synergetic strengthening in selectively laser melted austenitic stainless steel. Scr. Mater. 209, 114359. https://doi.org/10.1016/j.scriptamat.2021.114359

Lee, D.-H., Sun, B., Lee, S., Ponge, D., Jägle, E.A., Raabe, D., 2021. Comparative study of hydrogen embrittlement resistance between additively and conventionally manufactured 304L austenitic stainless steels. Mater. Sci. Eng. A 803, 140499. https://doi.org/10.1016/j.msea.2020.140499

Lee, D.-H., Lee, J.-A., Seok, M.-Y., Baek, U.B., Nahm, S.H., Jang, J., 2014a. Stress-dependent hardening-to-softening transition of hydrogen effects in nanoindentation of a linepipe steel. Int. J. Hydrogen Energy 39, 1897–1902. https://doi.org/10.1016/j.ijhydene.2013.11.060

Lee, J., Park, C., Park, H., Kang, N., 2020. Effective hydrogen diffusion coefficient for CoCrFeMnNi high-entropy alloy and microstructural behaviors after hydrogen permeation. Int. J. Hydrogen Energy 45, 10227–10232. https://doi.org/10.1016/j.ijhydene.2020.02.012

Lee, S.-I., Lee, J.-M., Lee, S.-Y., Kim, H.-J., Suh, J.-Y., Shim, J.-H., Baek, U.-B., Nahm, S.-H., Lee, J., Hwang, B., 2019. Tensile and fracture behaviors of austenitic high-manganese steels subject to different hydrogen embrittlement test methods. Mater. Sci. Eng. A 766, 138367. https://doi.org/10.1016/j.msea.2019.138367

Lee, S.K., Yun, S.-H., Joo, H.G., Noh, S.J., 2014b. Deuterium transport and isotope effects in type 316L stainless steel at high temperatures for nuclear fusion and nuclear hydrogen technology applications. Curr. Appl. Phys. 14, 1385–1388. https://doi.org/10.1016/j.cap.2014.08.006

Lee, S.-M., Lee, J.-Y., 1986. The trapping and transport phenomena of hydrogen in nickel. Metall. Trans. A 17, 181–187. https://doi.org/10.1007/BF02643893

Li, S., Li, Y., Lo, Y.C., Neeraj, T., Srinivasan, R., Ding, X., Sun, J., Qi, L., Gumbsch, P., Li, J., 2015. The interaction of dislocations and hydrogen-vacancy complexes and its importance for deformation-induced proto nano-voids formation in α-Fe. Int. J. Plast. 74, 175–191. https://doi.org/10.1016/J.IJPLAS.2015.05.017

Li, S.-H., Zhao, Y., Kumar, P., Ramamurty, U., 2022a. Effect of initial dislocation density on the plastic deformation response of 316L stainless steel manufactured by directed energy deposition. Mater. Sci. Eng. A 851, 143591. https://doi.org/10.1016/J.MSEA.2022.143591

Li, S.-H., Zhao, Y., Radhakrishnan, J., Ramamurty, U., 2022b. A micropillar compression investigation into the plastic flow properties of additively manufactured alloys. Acta Mater. 240, 118290. https://doi.org/10.1016/j.actamat.2022.118290

Li, X., Yin, J., Zhang, J., Wang, Y., Song, X., Zhang, Y., Ren, X., 2022c. Hydrogen embrittlement and failure mechanisms of multi-principal element alloys: A review. J. Mater. Sci. Technol. 122, 20–32. https://doi.org/10.1016/j.jmst.2022.01.008

Li, Y.X., Nutor, R.K., Zhao, Q.K., Zhang, X.P., Cao, Q.P., Sohn, S.S., Wang, X.D., Ding, S.Q., Zhang, D.X., Zhou, H.F., Wang, J.W., Jiang, J.Z., 2023. Unraveling the deformation behavior of the Fe45Co25Ni10V20 high entropy alloy. Int. J. Plast. 165, 103619. https://doi.org/10.1016/j.ijplas.2023.103619

Li, Y., Li, W., Min, N., Liu, H., Jin, X., 2020. Homogeneous elasto-plastic deformation and improved strain compatibility between austenite and ferrite in a co-precipitation hardened medium Mn steel with enhanced hydrogen embrittlement resistance. Int. J. Plast. 133, 102805. https://doi.org/10.1016/j.ijplas.2020.102805

Lin, J., Chen, F., Liu, F., Xu, D., Gao, J., Tang, X., 2020. Hydrogen permeation behavior and hydrogen-induced defects in 316L stainless steels manufactured by additive manufacturing. Mater. Chem. Phys. 250, 123038. https://doi.org/10.1016/j.matchemphys.2020.123038

Lin, Y.-T., An, X., Zhu, Z., Nai, M.L.S., Tsai, C.-W., Yen, H.W., 2022. Effect of cell wall on hydrogen response in CoCrFeMnNi high-entropy alloy additively manufactured by selective laser melting. J. Alloys Compd. 925, 166735. https://doi.org/10.1016/j.jallcom.2022.166735

Liu, Q., Atrens, A.D., Shi, Z., Verbeken, K., Atrens, A., 2014. Determination of the hydrogen fugacity during electrolytic charging of steel. Corros. Sci. 87, 239–258. https://doi.org/10.1016/j.corsci.2014.06.033

Lu, X., Ma, Y., Zamanzade, M., Deng, Y., Wang, D., Bleck, W., Song, W.W., Barnoush, A., 2019. Insight into hydrogen effect on a duplex medium-Mn steel revealed by in-situ nanoindentation test. Int. J. Hydrogen Energy 44, 20545–20551. https://doi.org/10.1016/J.IJHYDENE.2019.04.290

Marques, S.C., Castilho, A.V., dos Santos, D.S., 2021. Effect of alloying elements on the hydrogen diffusion and trapping in high entropy alloys. Scr. Mater. 201, 113957. https://doi.org/10.1016/j.scriptamat.2021.113957

Matsui, H., Kimura, H., Kimura, A., 1979. The effect of hydrogen on the mechanical properties of high purity iron III. The dependence of softening in specimen size and charging current density. Mater. Sci. Eng. 40, 227–234. https://doi.org/10.1016/0025-5416(79)90193-9

Miracle, D.B., Senkov, O.N., 2017. A critical review of high entropy alloys and related concepts. Acta Mater. https://doi.org/10.1016/j.actamat.2016.08.081

Nazarov, R., Hickel, T., Neugebauer, J., 2010. First-principles study of the thermodynamics of hydrogen-vacancy interaction in fcc iron. Phys. Rev. B - Condens. Matter Mater. Phys. 82, 1–11. https://doi.org/10.1103/PhysRevB.82.224104

Nibur, K.A., Bahr, D.F., Somerday, B.P., 2006. Hydrogen effects on dislocation activity in austenitic stainless steel. Acta Mater. 54, 2677–2684. https://doi.org/10.1016/j.actamat.2006.02.007

Oliver, W.C., Pharr, G.M., 2004. Measurement of hardness and elastic modulus by instrumented indentation: Advances in understanding and refinements to methodology. J. Mater. Res. 19, 3–20. https://doi.org/10.1557/jmr.2004.19.1.3

Oliver, W.C., Pharr, G.M., 1992. An improved technique for determining hardness and elastic modulus using load and displacement sensing indentation experiments. J. Mater. Res. 7, 1564–1583. https://doi.org/10.1557/JMR.1992.1564

Oudriss, A., Creus, J., Bouhattate, J., Conforto, E., Berziou, C., Savall, C., Feaugas, X., 2012. Grain size and grain-boundary effects on diffusion and trapping of hydrogen in pure nickel. Acta Mater. 60, 6814-6828. https://doi.org/10.1016/j.actamat.2012.09.004

Park, J.-M., Zhao, Y., Voisin, T., Lee, D.-H., Komazaki, S., Ko, Y., Kim, D.-I., Suh, J.-Y., Han, H.N., Wang, Y.M., Ramamurty, U., Jang, J., 2021. Hydrogen uptake and its influence in selective laser melted austenitic stainless steel: A nanoindentation study. Scr. Mater. 194, 113718. https://doi.org/10.1016/j.scriptamat.2020.113718

Perdew, J.P., Burke, K., Wang, Y., 1996. Generalized gradient approximation for the exchange-correlation hole of a many-electron system. Phys. Rev. B 54, 16533–16539. https://doi.org/10.1103/PhysRevB.54.16533

Pontini, A.E., Hermida, J.D., 1997. X-Ray diffraction measurement of the stacking fault energy reduction induced by hydrogen in an AISI 304 steel. Scr. Mater. 37, 1831–1837. https://doi.org/10.1016/S1359-6462(97)00332-1

Qu, W., Gu, C., Zheng, J., Zhao, Y., Hua, Z., 2019. Effect of plastic deformation at room temperature on hydrogen diffusion of S30408. Int. J. Hydrogen Energy 44, 8751–8758.

https://doi.org/10.1016/j.ijhydene.2018.07.156

Ren, X.L., Shi, P.H., Zhang, W.W., Wu, X.Y., Xu, Q., Wang, Y.X., 2019. Swamps of hydrogen in equiatomic FeCuCrMnMo alloys: First-principles calculations. Acta Mater. 180, 189–198. https://doi.org/10.1016/j.actamat.2019.09.014

Ryu, J.H., Chun, Y.S., Lee, C.S., Bhadeshia, H.K.D.H., Suh, D.W., 2012. Effect of deformation on hydrogen trapping and effusion in TRIP-assisted steel. Acta Mater. 60, 4085–4092. https://doi.org/10.1016/j.actamat.2012.04.010

San Marchi, C., Somerday, B.P., Robinson, S.L., 2007. Permeability, solubility and diffusivity of hydrogen isotopes in stainless steels at high gas pressures. Int. J. Hydrogen Energy 32, 100–116. https://doi.org/10.1016/j.ijhydene.2006.05.008

Soundararajan, C.K., Wang, D., Vinogradov, A., 2023. Effect of hydrogen on nanomechanical properties of Inconel 625 studied using in-situ electrochemical nanoindentation technique. J. Alloys Compd. 948, 169742. https://doi.org/10.1016/J.JALLCOM.2023.169742

Soundararajan, C.K., Luo, H., Raabe, D., Li, Z., 2020. Hydrogen resistance of a 1 GPa strong equiatomic CoCrNi medium entropy alloy. Corros. Sci. 167, 108510. https://doi.org/10.1016/j.corsci.2020.108510

Tarzimoghadam, Z., Rohwerder, M., Merzlikin, S.V., Bashir, A., Yedra, L., Eswara, S., Ponge, D., Raabe, D., 2016. Multi-scale and spatially resolved hydrogen mapping in a Ni–Nb model alloy reveals the role of the δ phase in hydrogen embrittlement of alloy 718. Acta Mater. 109, 69–81. https://doi.org/10.1016/j.actamat.2016.02.053

Tsai, K.-Y., Tsai, M.-H., Yeh, J.-W., 2013. Sluggish diffusion in Co–Cr–Fe–Mn–Ni high-entropy alloys. Acta Mater. 61, 4887–4897. https://doi.org/10.1016/j.actamat.2013.04.058

Tsong-Pyng, P., Altstetter, C.J., 1986. Effects of deformation on hydrogen permeation in austenitic stainless steels. Acta Metall. 34, 1771–1781. https://doi.org/10.1016/0001-6160(86)90123-9

Uhlemann, M., Pound, B.G., 1998. Diffusivity, solubility and trapping behavior of hydrogen in alloys 600, 690tt and 800. Corros. Sci. 40, 645–662. https://doi.org/10.1016/S0010-938X(97)00167-4

Wang, D., Lu, X., Lin, M., Wan, D., Li, Z., He, J., Johnsen, R., 2022. Understanding the hydrogen effect on pop-in behavior of an equiatomic high-entropy alloy during in-situ nanoindentation. J. Mater. Sci. Technol. 98, 118–122. https://doi.org/10.1016/J.JMST.2021.04.060

Wang, Y.M., Voisin, T., McKeown, J.T., Ye, J., Calta, N.P., Li, Z., Zeng, Z., Zhang, Y., Chen, W., Roehling, T.T., Ott, R.T., Santala, M.K., Depond, P.J., Matthews, M.J., Hamza, A. V., Zhu, T., 2018. Additively manufactured hierarchical stainless steels with high strength and ductility. Nat. Mater. 17, 63–71. https://doi.org/10.1038/nmat5021

Wei, D., Gong, W., Tsuru, T., Kawasaki, T., Harjo, S., Cai, B., Liaw, P.K., Kato, H., 2022. Mechanical behaviors of equiatomic and near-equiatomic face-centered-cubic phase high-entropy alloys probed using in situ neutron diffraction. Int. J. Plast. 158, 103417. https://doi.org/10.1016/j.ijplas.2022.103417

Wen, M., Fukuyama, S., Yokogawa, K., 2004. Hydrogen-affected cross-slip process in fcc nickel. Phys. Rev. B 69, 174108. https://doi.org/10.1103/PhysRevB.69.174108

Xie, Z., Wang, Y., Lu, C., Dai, L., 2021. Sluggish hydrogen diffusion and hydrogen decreasing stacking fault energy in a high-entropy alloy. Mater. Today Commun. 26, 101902. https://doi.org/10.1016/j.mtcomm.2020.101902

Xiukui, S., Jian, X., Yiyi, L., 1989. Hydrogen permeation behaviour in austenitic stainless steels. Mater. Sci. Eng. A 114, 179–187. https://doi.org/10.1016/0921-5093(89)90857-5

Zhang, L., Wen, M., Imade, M., Fukuyama, S., Yokogawa, K., 2008. Effect of nickel equivalent on hydrogen gas embrittlement of austenitic stainless steels based on type 316 at low temperatures. Acta Mater. 56, 3414–3421. https://doi.org/10.1016/j.actamat.2008.03.022

Zhang, X., Gui, Y., Lai, M., Lu, X., Gu, J., Wang, F., Yang, T., Wang, Z., Song, M., 2023. Enhanced strength-ductility synergy of medium-entropy alloys via multiple level gradient structures. Int. J. Plast. 164, 103592. https://doi.org/10.1016/J.IJPLAS.2023.103592

Zhang, Z., Moore, K.L., McMahon, G., Morana, R., Preuss, M., 2019. On the role of precipitates in hydrogen trapping and hydrogen embrittlement of a nickel-based superalloy. Corros. Sci. 146, 58–69. https://doi.org/10.1016/j.corsci.2018.10.019

Zhao, S., Berry-Gair, J., Li, W., Guan, G., Yang, M., Li, J., Lai, F., Corà, F., Holt, K., Brett, D.J.L., He, G., Parkin, I.P., 2020. Hydrogen Evolution: The Role of Phosphate Group in Doped Cobalt Molybdate: Improved Electrocatalytic Hydrogen Evolution Performance (Adv. Sci. 12/2020). Adv. Sci. 7, 2070067. https://doi.org/10.1002/advs.202070067

Zhao, Y., Park, J.-M., Lee, D.-H., Song, E.J., Suh, J.-Y., Ramamurty, U., Jang, J., 2019. Influences of hydrogen charging method on the hydrogen distribution and nanomechanical properties of face-centered cubic high-entropy alloy: A comparative study. Scr. Mater. 168, 76–80. https://doi.org/10.1016/j.scriptamat.2019.04.025

Zhao, Y., Lee, D.-H., Lee, J.-A., Kim, W.-J., Han, H.N., Ramamurty, U., Suh, J.-Y., Jang, J., 2017a. Hydrogen-induced nanohardness variations in a CoCrFeMnNi high-entropy alloy. Int. J. Hydrogen Energy 42, 12015–12021. https://doi.org/10.1016/j.ijhydene.2017.02.061

Zhao, Y., Lee, D.-H., Seok, M.-Y., Lee, J.-A., Phaniraj, M.P., Suh, J.-Y., Ha, H.-Y., Kim, J.-Y., Ramamurty, U., Jang, J., 2017b. Resistance of CoCrFeMnNi high-entropy alloy to gaseous hydrogen embrittlement. Scr. Mater. 135, 54–58. https://doi.org/10.1016/j.scriptamat.2017.03.029

Zhao, Y., Seok, M.-Y., Lee, D.-H., Lee, J.-A., Suh, J.-Y., Jang, J., 2016. Hydrogen-induced softening in nanocrystalline Ni investigated by nanoindentation. Philos. Mag. 96, 3442–3450. https://doi.org/10.1080/14786435.2016.1159743

Zhao, Y., Seok, M.-Y., Choi, I.-C., Lee, Y.-H., Park, S.-J., Ramamurty, U., Suh, J.-Y., Jang, J., 2015. The role of hydrogen in hardening/softening steel: Influence of the charging process. Scr. Mater. 107, 46–49. https://doi.org/10.1016/j.scriptamat.2015.05.017

Zhao, Y., Choi, I.-C., Seok, M.-Y., Ramamurty, U., Suh, J.-Y., Jang, J., 2014. Hydrogen-induced hardening and softening of Ni–Nb–Zr amorphous alloys: Dependence on the Zr content. Scr. Mater. 93, 56–59. https://doi.org/10.1016/j.scriptamat.2014.08.029

Zhou, X., Marchand, D., McDowell, D.L., Zhu, T., Song, J., 2016. Chemomechanical Origin of Hydrogen Trapping at Grain Boundaries in fcc Metals. Phys. Rev. Lett. 116, 075502. https://doi.org/10.1103/PhysRevLett.116.075502

Zhou, X.-Y., Zhu, J.-H., Wu, Y., Yang, X.-S., Lookman, T., Wu, H.-H., 2022. Machine learning assisted design of FeCoNiCrMn high-entropy alloys with ultra-low hydrogen diffusion coefficients. Acta Mater. 224, 117535. https://doi.org/10.1016/j.actamat.2021.117535

Zhu, Y., Li, Z., Huang, M., Fan, H., 2017. Study on interactions of an edge dislocation with vacancy-H complex by atomistic modelling. Int. J. Plast. 92, 31–44. https://doi.org/10.1016/j.ijplas.2017.03.003